J. Fluid Mech. (2004), *vol.* 516, *pp.* 125–154.
DOI: 10.1017/S002211200400059X Printed in the United Kingdom

Kinematics of the stationary helical vortex mode in Taylor–Couette–Poiseuille Flow

By L. GUY RAGUIN[1,2] AND JOHN G. GEORGIADIS[1,2,3]†

[1]Laboratory for Quantitative Visualization in Energetics, Department of Mechanical and Industrial Engineering, University of Illinois at Urbana-Champaign, 1206 West Green Street, Urbana, IL 61801, USA

[2]NSF Sci. & Tech. Center of Advanced Materials for Purification of Water with Systems, University of Illinois at Urbana-Champaign, Urbana, IL 61801, USA

[3]Bioengineering Department, University of Illinois at Urbana-Champaign, 1304 West Springfield Ave., Urbana, IL 61801, USA

(Received 12 March 2003 and in revised form 17 May 2004)

We reconstruct a kinematically admissible (volume-preserving) three-dimensional velocity field corresponding to the stationary helical vortex (SHV) mode which is observed in the Taylor–Couette–Poiseuille (TCP) system with a ratio of inner to outer cylinder radii of 0.5 and a length to annulus gap ratio of 16, starting from experimental data obtained via magnetic resonance imaging (MRI) for $Re = 11.14$ and $Ta^{1/2} = 170$ in water. The goal of the present work is to provide a complete kinematic representation of a strongly nonlinear duct flow that is of importance in the fields of mixing and segregation, as well as in the study of the kinematic structure of three-dimensional flows. By a judicious choice of a set of global basis functions that exploit the helical symmetry of SHV, an analytical approximation of the streamfunction is obtained despite the coarse MRI data and the non-uniform distribution of measurement error. This approximation is given in terms of a truncated series of smooth functions that converges weakly in L_2, and the reconstruction method is directly applicable to three-dimensional incompressible flows that possess a continuous volume-preserving symmetry. The SHV flow structure consists of a pair of asymmetric counter-rotating helical cells in a double helix structure, foliated with invariant helically symmetric surfaces containing fibre-like fluid particle orbits wrapped around the inner cylinder. Imposing general topological constraints, juxtaposing SHV with neighbouring hydrodynamic modes such as the propagating Taylor vortex flow and direct numerical simulation help corroborate the validity of the reconstruction of the SHV flow field. The kinematically admissible flow field obeys the Navier–Stokes equations with 10% accuracy, which is consistent with experimental error, and has the same flow portrait as the numerically computed flow. Global analysis of the SHV mode indicates that it corresponds to a minimum in dissipation and mixing in comparison with a wide class of perturbed neighbouring modes; hence it is a candidate for the study of particle segregation. To our knowledge, the present study reports the first synthesis of a physically realizable complex open flow that can be represented by an integrable Hamiltonian system starting from point-wise experimental data and using solely kinematic constraints.

† Author to whom correspondence should be addressed: georgia@uiuc.edu

1. Introduction

The study of geometric fluid mechanics forms a nexus between the broad field of nonlinear analysis (Abraham, Marsden & Ratiu 1988) and the more specialized field of chaotic mixing (Ottino 1989). There has been an increasing awareness of the role that chaotic flows can play in the creation of order, in terms of persistent spatial patterns (Rothstein, Henry & Gollub 1999) or segregation (Benczik, Toroczkai & Tel 2002) of a dispersed phase, rather than mixing or stirring of the flow. The majority of the chaotic fluid mechanical systems used in the study of mixing or separation are obtained by perturbing simpler flows, such as two-dimensional steady flows (e.g. Stokes flows used by Jana, Metcalfe & Ottino 1994) or weakly nonlinear flows (Ashwin & King 1997) based on the narrow-gap asymptotic approximation of Taylor–Couette flows performed by Davey, DiPrima & Stuart (1968). Ashwin & King (1995) underline the paucity of analytical representations of three-dimensional flows used to study Lagrangian chaos. Owing to their complexity, such flows are very difficult to reconstruct from numerical or experimental data. More importantly, as Ashwin & King (1995) point out, there is a risk that flows that do not obey correct kinematics might introduce spurious chaotic behaviour stemming from Lagrangian property errors.

In this manuscript, we pursue the thesis that it is possible to construct an accurate analytical representation of a certain class of steady three-dimensional flow fields by imposing rigourous kinematic constraints on relatively coarse velocity measurements obtained experimentally or numerically. Toward this end, we pursue the study of the stationary helical vortex mode, a strongly nonlinear flow appearing in the Taylor–Couette–Poiseuille system, for which experimental measurements of the velocity field were obtained via magnetic resonance imaging, and a corroborating numerical validation became available. The velocity reconstruction methodology is related to the recent work by Raguin (2004) and Raguin & Georgiadis (2004*a*), who developed a physics-based dynamic imaging method that allows the extraction of general irrotational or divergence-free velocity fields from sparse experimental data sets. Our goals here extend beyond the high-resolution reconstruction of the SHV mode, which is a rather specialized flow. We lay here the foundation for the analytical study of a class of real three-dimensional two-phase flows, which promise rich fluid dynamics involving chaotic mixing or segregation. Imposing correct kinematics (such as strict mass conservation) during the reconstruction of the Eulerian velocity field contributes to the accuracy with which critical Lagrangian properties of such flows can be evaluated.

1.1. *The Taylor–Couette–Poiseuille system*

When a viscous fluid is placed in a closed annular cavity between a rotating inner cylinder and a fixed coaxial outer cylinder, the base (Couette) flow becomes unstable as soon as the rotation speed of the inner cylinder exceeds a critical value. This instability gives rise to a hydrodynamic mode possessing an $\mathbf{SO}(2) \times \mathbf{O}(2)$ symmetry and characterized by stationary axisymmetric counter-rotating vortices that fill the whole annular region. These toroidal vortices are the result of an absolute instability and the associated flow is commonly referred to as Taylor–Couette (TC) flow. When a through-flow driven by a pressure gradient along the centreline is added, the TC flow loses the $\mathbf{O}(2)$ symmetry (invariance to continuous translations in the axial direction) and the resulting open system can now exhibit both convective and absolute instabilities. The base flow consists of a superposition of circular Couette flow and annular Poiseuille flow and is thus appropriately labelled Couette–Poiseuille (CP) flow. The

axial through-flow suppresses the basic stationary instability, and as the axial pressure gradient increases while the rotation speed of the inner cylinder is held fixed, the first bifurcation gives rise to a travelling train of axisymmetric Taylor vortices, commonly referred to as propagating Taylor vortices (PTV). Henceforth, the term Taylor–Couette–Poiseuille (TCP) flow is used to refer to all hydrodynamic phenomena pertaining to the open system described above.

The hydrodynamics of TCP flow is described by two dimensionless parameters, the Taylor number Ta and the axial Reynolds number Re, which correspond to the rotational speed of the inner cylinder and the imposed axial flow rate, respectively:

$$Ta = \frac{4\eta^2}{1-\eta^2}\left(\frac{\Omega}{\nu}\right)^2 (R_2 - R_1)^4, \quad Re = \frac{(R_2 - R_1)U}{\nu}. \tag{1.1a, b}$$

R_1 and R_2 are the inner and outer cylinder radii, Ω is the inner cylinder angular velocity, U denotes the mean axial velocity imposed by the through-flow, and ν is the fluid kinematic viscosity. Two geometric dimensionless parameters complete the description of TCP flow. They consist of the ratio of inner to outer cylinder radii, $\eta = R_1/R_2$, and the ratio of the length L of the cylinders to the annulus gap, called the aspect ratio, $\Gamma = L/(R_2 - R_1)$.

At the limit $\Gamma \to \infty$, the inlet and outlet regions of the flow do not affect the core of the flow in closed systems. End effects can be neglected for TC systems with $\Gamma > 10$, according to Snyder (1969). However, there is no such criterion for TCP systems, one possible reason being that there is a strong influence of the imposed inlet axial velocity profile and entrance conditions in TCP flow. Regarding the effect of the radii ratio η, Coles (1965) determined, also for TC flow, that if η is greater than 0.714, a secondary instability occurs at a sufficiently high rotation speed of the inner cylinder. The critical value of $\eta = 0.714$ was derived analytically by Davey (1962). The new instability takes the form of wavy Taylor vortices characterized by an oscillation pattern that is superposed on the Taylor vortices in the azimuthal direction. There have been no systematic studies of secondary bifurcation in TCP flow, with the exception of studies concerning relatively narrow gaps by Schwarz, Springett & Donnelly (1964), Bühler & Polifke (1990), Lueptow, Docter & Min (1992), and Wereley & Lueptow (1999). The difficulties with the TCP problem stem from the lack of analytical description of the PTV modes and are compounded by the presence of both absolute and convective instabilities. While absolutely unstable modes are insensitive to initial conditions and system size, in the convectively unstable regime the growing flow patterns depend on initial conditions and on the spatial distribution of perturbations (Büchel, Lücke & Schmitz 1996). Entrance conditions that shape the form of the perturbations entering the system may excite one mode preferentially while inhibiting the growth of another, and there is very little control of these perturbations in experiments.

1.2. *The stationary helical vortex (SHV) mode of TCP*

Among the secondary instabilities in the TCP system observed as the dynamic parameters Re and Ta are varied, the stationary helical vortex (SHV) mode has received very little attention. The spatial structure of the simplest SHV mode consists of two stationary counter-rotating helical vortices in a double helix structure, winding around the inner cylinder and filling the whole annular cavity (azimuthal wavenumber equal to unity). By fixing the speed of the inner cylinder rotation, the SHV mode appears as a secondary flow bifurcation after the primary bifurcation from CP flow to PTV flow,

and is followed by another bifurcation to a disordered PTV mode. The term 'bifurcation' here refers to the abrupt changes in the qualitative character of the solutions of the Navier–Stokes equations (cf. Drazin & Reid 1981). The transition from CP flow to PTV flow corresponds to a symmetry change from axisymmetry (**SO**(2) symmetry about the centreline) and continuous translational invariance in the axial direction, to periodicity in the axial direction ($\mathbf{Z}_2$), while keeping the azimuthal **SO**(2) symmetry. The secondary bifurcation to the SHV mode yields a symmetry change from axisymmetry to helical symmetry, and both modes need two independent coordinates to fully describe them. These transitions around the SHV mode and this particular mode were experimentally observed and reported by Lueptow *et al.* (1992) who proposed a map of the flow regimes occurring in their relatively narrow-gap apparatus ($\eta = 0.848$) using visual and optical methods. Tsameret & Steinberg (1994) also described nonlinear mode interactions consisting of temporal alternation of two or more flow patterns, and mixed phases characterized by the superposition of two or more flow patterns near the region of existence of the SHV mode for a wider-gap test section ($\eta = 0.707$ and 0.77). Finally, Moser, Raguin & Georgiadis (2001*b*) observed an additional nonlinear mixed mode consisting of the juxtaposition of the SHV mode near the inlet and the PTV mode near the outlet.

To our knowledge, the first experimental observation of the SHV mode was reported by Bühler & Polifke (1990). The results of that study however contrast with all other subsequent studies of TCP flow, and with the flow regimes map reported by Lueptow *et al.* (1992) in particular. Bühler & Polifke (1990) observed a multitude of helical vortex modes, with azimuthal wavenumbers as high as three, corresponding to six helical vortices winding around the inner cylinder, either stationary or travelling in the same direction as or opposite to the mean axial flow. The travelling helical modes reported by Lueptow *et al.* (1992) propagate only in the same direction as the mean flow and have helix angles of less than 5°, which, given the geometry of their apparatus, can only correspond to an azimuthal wavenumber equal to unity. The reason for these apparently contradicting observations cannot be found in the difference in the geometry of the experimental annular regions (the former had $\eta = 0.8$ and $\Gamma = 20$, and the latter $\eta = 0.848$ and $\Gamma = 41$), but rather in the flow entrance conditions. While Lueptow *et al.* (1992), as well as most researchers studying the TCP system, used a honeycomb section before the entrance to the annular region to straighten the incoming axial flow, Bühler & Polifke (1990) introduced a flow swirl at the inlet. Since the TCP system is open and thus sensitive to inlet boundary conditions, this modification of the experiment is expected to have dramatic consequences for the evolution of the nonlinear states in TCP flow. In other words, Bühler & Polifke (1990) may have studied a modification of the TCP system, hence their results cannot be compared to most of the other research on the subject.

The practical urge to explore the SHV mode is based on much greater experimental capabilities than have previously been available. In an earlier magnetic resonance imaging (MRI) study, Moser *et al.* (2000*c*) and Moser *et al.* (2001*b*) detected the simplest SHV mode (azimuthal wave-number unity) and reported on its breakdown and subsequent competition with the PTV mode. It was verified that the three-dimensional velocity field of the pure SHV mode is time-independent and possesses a helical symmetry with axial wavelength $\lambda \simeq 2(R_2 - R_1)$. The bulk helical symmetry is broken near the inlet and outlet boundaries where the flow accommodates the no-slip boundary condition via Ekman layers. The revealed continuous symmetry makes the SHV regime quite attractive for both experimental and analytical studies. Moreover, the presence of a stationary nonlinear mode, such as SHV, in regions of

the bifurcation space surrounded by unsteady mode domains is of particular interest and relevance in the study of mixing or separation processes using swirling flows (cf. Ottino 1989; Ameer *et al.* 1999).

1.3. *Outline*

Starting from the experimental data of the SHV mode obtained via MRI velocimetry by Moser *et al.* (2001*b*), the reconstruction process of the three-dimensional velocity field and its analytical approximation will be discussed in the following section. A systematic theoretical investigation of the kinematic properties of the approximated SHV velocity field is given in § 3, including the relationship between the SHV mode and the neighbouring PTV mode. The final section addresses the connection between the global topological properties of the SHV mode, passive scalar transport, and mechanical energy dissipation.

2. Methodology

2.1. *MRI velocimetry*

Magnetic resonance imaging is a tomographic imaging technique that makes it possible to image arbitrary cross-sections through the interior of rotating systems and obtain information about the velocity profiles directly. Obtaining accurate full-field velocity measurements in domains delineated by topologically complex solid surfaces is impossible via optical methods, especially if these surfaces obstruct the field of view. In the general case of rotating systems (mixers or turbines) and owing to the practical limitations of attempts to fully compensate for light ray distortion or scattering, optical methods can only image from planes not intersected by the rotating blades during the image acquisition phase. Although great gains in the elimination of perspective effects have been achieved with the use of multiple cameras, the flow between the blades or on a meridional plane containing the axis of the rotor is practically inaccessible. The state-of-the-art in stereoscopic optical imaging is represented by two examples: Hill, Sharp & Adrian (2000) employed particle image velocimetry (PIV) to reconstruct the turbulent flow outside the inter-blade domain of a Rushton turbine, and Bohl, Koochesfahani & Olson (2001) used molecular tagging velocimetry to obtain three-dimensional velocity measurements in the vicinity of a mixer propeller. Among non-optical techniques allowing flow imaging through such essentially opaque systems, only MRI has achieved a level of sophistication and spatial resolution that allows quantitative visualization of the three-dimensional flow field in such systems. Owing to rapid improvements in MRI scanner technology and our growing experience with magnetically compatible test sections, flow-sectioning experiments such as the one reported here can be performed on a more cost-effective basis than those requiring optical techniques.

The advantages that MRI velocimetry offers in terms of non-invasiveness, choosing the contrast mechanism and the field of view, are somewhat offset by a loss in accuracy. While optical techniques such as laser Doppler velocimetry (LDV) and PIV can provide an accuracy on the order of 1%, MRI velocimetry exhibits a modest 10% accuracy in the case of phase-contrast techniques (cf. Moser *et al.* 2000*b*). Spin-tagging methods are even less accurate unless they are coupled with an automated post-processing tool, such as an optical flow code, which lowers the average error to less than 10% for a simple annular Poiseuille flow (cf. Moser, Georgiadis & Buckius 2001*a*). This estimate of 10% accuracy was obtained by a point-wise comparison with analytical or numerical solutions, and it represents a compromise between spatial

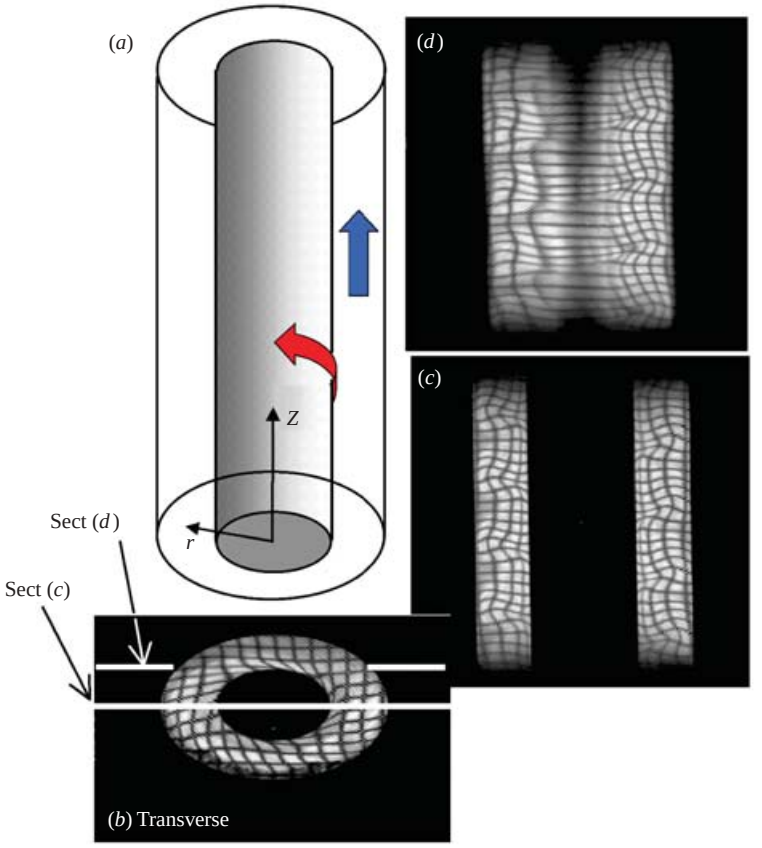

FIGURE 1. MRI visualization of the SHV mode using the spin-tagging spin-echo sequence. (*a*) Schematic of the TCP system; (*b*) transverse section of the SHV mode located at $z = 75$ mm from the flow entrance; (*c*) meridional section of the SHV mode; (*d*) extra-axial section of the SHV mode.

resolution and time constraints (cf. Moser *et al.* 2000*b*; Moser, Georgiadis & Buckius 2000*a*). In order to recover some of the accuracy in MRI velocimetry, we explore the possibility of using physical (i.e. fluid mechanical) constraints to supplement the post-processing step. In the present study, we propose a method to approximate the velocity data with analytical functions that are solenoidal and satisfy the boundary conditions exactly. A general model-based dynamic imaging method that strictly enforces physical constraints has been developed by Raguin (2004) and Raguin & Georgiadis (2004*a*), and enables the reconstruction of physically admissible velocity fields from low-resolution velocimetry data.

While existing reconstruction procedures typically approximate experimental data by satisfying smoothness and physical constraints (such as mass conservation) in a 'weak' form, Raguin (2004) and Raguin & Georgiadis (2004*a*) employ the physics of the flow formally by projecting the data onto a set of functions that satisfy a set of fluid mechanical constraints exactly. This set of decomposition functions can be derived analytically for relatively simple flow domains (as is the case here), or obtained numerically using images of the flow domain and computational fluid dynamics when the boundaries are complex (cf. Raguin *et al.* 2004). An experimentally or numerically determined velocity field $\boldsymbol{V}$ can be decomposed into a reference flow field profile $\boldsymbol{V}^{\mathrm{ref}}$

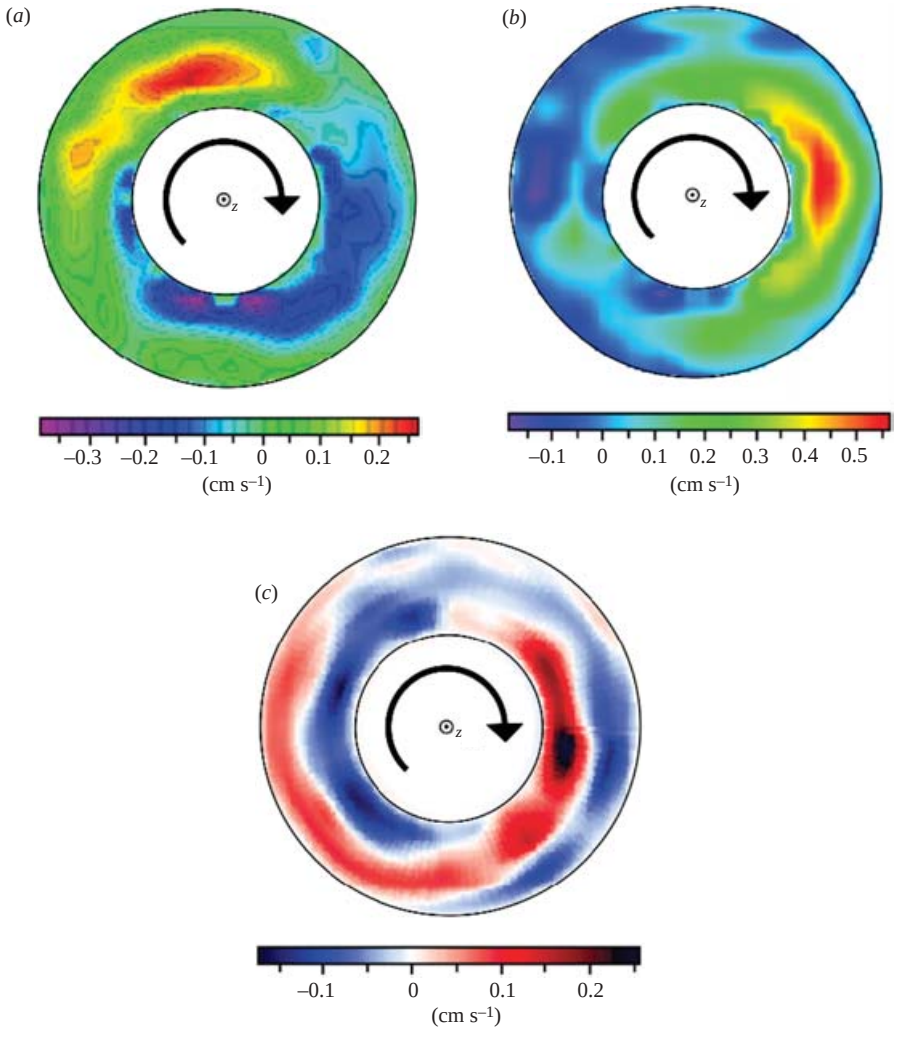

FIGURE 2. Reconstructed three-dimensional velocity field fluctuations (*a*) v_r, (*b*) v_θ, and (*c*) v_z in the (r, θ)-plane for SHV flow relative to the Couette–Poiseuille flow field. The inner cylinder rotates in the clockwise direction, while the mean axial flow is in the direction coming out of the page.

that accommodates the average properties of the velocity field, and an additional velocity field $\boldsymbol{v}$ satisfying homogeneous boundary conditions. Exploiting the potential spatial symmetries and stationarity of the flow, the velocity reconstruction problem can be represented mathematically by a homogeneous problem. For instance, if a three-dimensional volume-preserving velocity field consists of travelling waves or is stationary, and additionally possesses a continuous symmetry (e.g. translational invariance, axisymmetry), a streamfunction can be defined in a two-dimensional reduced coordinate system. In that case, a complete set of orthogonal basis functions (or at least a representative set of approximation functions) in the reduced coordinate system may be constructed, such that each approximation function satisfies all the kinematic constraints (incompressible flow, no-slip boundary conditions). This set of approximation functions can then be used to construct an analytical approximation for $\boldsymbol{v}$ in

terms of a series expansion. The series converges in L_2, and is truncated according to the convergence of a discrete least-squares error with respect to the point-wise experimental or numerical velocity data and a volume-averaged viscous dissipation function used to avoid spurious oscillations in the approximated velocity field. The following consists of the specific application to the reconstruction of the SHV velocity field, taking advantage of the helical symmetry and steadiness of the flow.

2.2. *MRI reconstruction of SHV*

By visualizing the displacement of grid patterns of (magnetically tagged) material lines in transverse and meridional sections of the TCP flow with a fast MRI technique developed by Moser *et al.* (2000*c*), the three-dimensional velocity field of the SHV mode was first described qualitatively by Moser *et al.* (2001*b*) for $Re = 11.14$ ($U = 1.1695\,\mathrm{mm\,s^{-1}}$) and $Ta^{1/2} = 170$ ($\Omega = 15.5$ r.p.m.). It is precisely this flow field that is revisited here, but from a quantitative viewpoint. The experimental test section has an annular region with $R_1 = 9.525$ mm, $R_2 = 19.05$ mm, $L = 152.4$ mm, which corresponds to $\Gamma = 16$ and $\eta = 0.5$. By convention, the z-axis is the common axis of the inner and outer cylinders and is oriented in the direction of the externally imposed through-flow, as shown in figure 1(*a*). The x- and y-velocity components (and subsequently r- and θ-components in cylindrical coordinates) are estimated using the displacement of the nodal points of Cartesian grids formed by material lines superimposed on five equidistant transverse slices, i.e. (x, y)-planes, roughly spanning one wavelength λ in the middle of the test section, cf. Moser *et al.* (2001*b*) and figure 1(*b*). The material grid resolution in the transverse sections is 13 by 13, and the image has a square pixel resolution of 0.117 mm. The z-component of the velocity field is similarly determined using the distortion of material grids encoded on meridional slices, i.e. (r, z)-planes as shown in figure 1(*c*), where the image resolution is 0.195 mm in the axial direction and 0.117 mm in the transverse direction. The axial wavelength, which is the helical pitch of the SHV velocity field, is determined from the meridional slices to be $\lambda \simeq 20$ mm. This value is consistent with the transverse velocity field obtained from the five available transverse slices, and it implies an overall helical symmetry in the SHV flow field $\boldsymbol{V}$ as follows:

$$\forall(\theta_0, z_0), \quad \boldsymbol{V}(r, \theta, z) = \boldsymbol{V}\left(r, \theta + 2\pi\frac{z - z_0}{\lambda}, z_0\right) = \boldsymbol{V}\left(r, \theta_0, z + \lambda\frac{\theta - \theta_0}{2\pi}\right). \tag{2.1}$$

The helical symmetry of the transverse velocity components is verified within the experimental error by rotating and comparing the velocity obtained on the five transverse slices. In addition, such symmetry is consistent with data from additional slices such as the extra-axial slice depicted in figure 1(*d*). The helical symmetry relation (2.1) implies that the three-dimensional velocity field can be reconstructed starting from the three independent velocity components in a single transverse slice at an arbitrary axial location z. It is convenient to decompose the full velocity field $\boldsymbol{V} = (V_r, V_\theta, V_z)$ into the CP velocity field $(0, V_\theta^{\mathrm{CP}}, V^{\mathrm{CP}}{}_z)$ taken as a reference, and a fluctuating field (v_r, v_θ, v_z), as follows:

$$(V_r, V_\theta, V_z) = \left(v_r, V_\theta^{\mathrm{CP}} + v_\theta, V_z^{\mathrm{CP}} + v_z\right) \tag{2.2}$$

where

$$V_\theta^{\mathrm{CP}}(r) = Ar + \frac{B}{r}, \quad V_z^{\mathrm{CP}}(r) = \frac{U}{E}\left[\frac{r^2}{(R_2 - R_1)^2} + C\ln\frac{r}{R_2 - R_1} + D\right], \tag{2.3}$$

and

$$\left.\begin{aligned} A &= -\frac{\Omega\eta^2}{1-\eta^2}, \quad B = \frac{\Omega R_2^2\eta^2}{1-\eta^2}, \quad C = \frac{1+\eta}{(1-\eta)\ln\eta}, \\ D &= C\ln(1-\eta) - \frac{1}{(1-\eta)^2}, \quad E = -\frac{1}{2}\left[1 + \frac{2\eta}{(1-\eta)^2} + C\right]. \end{aligned}\right\} \tag{2.4}$$

Figure 2 then shows the MRI measurements of (v_r, v_θ, v_z) represented on the transverse slice at $z = 0$ corresponding to a section at a distance of $0.45L$ into the annulus. The regions of maximum and minimum values of the radial velocity component v_r help locate the outflow and inflow regions separating the two counter-rotating helical vortices (figure 2*a*), while the features of the axial component v_z clearly indicate the helical structure of the SHV mode (figure 2*c*). The conservation of the axial flow rate is satisfied as the average of v_z over a cross-section is found to be about 0.5% of U, justifying the use of the Poiseuille profile as a reference velocity profile for V_z. Regarding the radial velocity component, the mean flux through any cylinder of radius r, i.e. the azimuthal average of V_r, should be zero, and thus, so should be the mean of V_r over a cross-section. Since V_r is acquired on a Cartesian grid, only the latter can be verified, and we find that the mean of V_r is 6% of U, which is satisfying given the 10% to 20% experimental error. In the θ-direction, there is no extrinsic conservation constraint, and we can merely report that the mean value of v_θ is about 74% of U. This indicates that the fluctuation velocity v_θ is not zero on average, and thus the Couette profile in the θ-direction is clearly not the mean profile. At this stage of the analysis, the Couette–Poiseuille profile is simply employed to handle the heterogeneous boundary conditions, and no assumptions are made about the mean values of the fluctuation field (v_r, v_θ, v_z).

2.3. *Analytical approximation of the SHV velocity field*

Faced with very coarse measurements and large measurement error, an analytical expression is sought to approximate the velocity fluctuations $\boldsymbol{v} = (v_r, v_\theta, v_z)$ over the whole annular region. Specifically, we employ the discrete least-squares method to fit the coefficients of a trial orthogonal function expansion, so that it satisfies certain constraints and minimizes an error-measuring norm. Given the geometry of the problem at hand, we seek to define the trial functions for each of the velocity components in cylindrical coordinates. No trial functions for all three velocity components could be readily found that inherently satisfy the continuity equation

$$\frac{1}{r}\frac{\partial}{\partial r}(r v_r) + \frac{1}{r}\frac{\partial v_\theta}{\partial\theta} + \frac{\partial v_z}{\partial z} = 0, \tag{2.5}$$

as well as the no-slip boundary conditions on the annular cavity walls

$$\boldsymbol{v}(R_1, \theta, z) = \boldsymbol{v}(R_2, \theta, z) = (0, 0, 0). \tag{2.6}$$

A number of possibilities are available depending on which constraints are enforced and which ones are relaxed. Ashwin & King (1995) enforced only approximately the continuity equation and relaxed the no-slip boundary conditions in their investigation of eccentric Taylor vortex flow. Using an asymptotic approximation for the velocity field that does not preserve volume can affect the characterization of critical points, especially elliptic points. Starting from the SHV measurements, we opt to construct a global approximation for the velocity field that satisfies all the kinematic constraints (symmetry, boundary conditions, and continuity equation), using the approach

developed by Raguin (2004) and Raguin & Georgiadis (2004*a*) and applied specifically to the SHV flow.

The starting point is to make full use of the helical symmetry of the SHV velocity field. Differentiating the right-hand side of (2.1) with respect to z, and choosing $z_0 = 0$ leads to

$$\frac{\partial v_i(r,\theta,z)}{\partial z} = \frac{2\pi}{\lambda}\frac{\partial v_i(r,\theta+2\pi z/\lambda,0)}{\partial \theta}, \quad i \in \{r,\theta,z\}. \tag{2.7}$$

By applying (2.7) for $i = z$, (2.5) can be rewritten as

$$\frac{1}{r}\frac{\partial}{\partial r}(r v_r) + \frac{1}{r}\frac{\partial v_\theta}{\partial \theta} + \frac{2\pi}{\lambda}\frac{\partial v_z}{\partial \theta} = 0. \tag{2.8}$$

Two alternative two-dimensional coordinate systems can then be introduced:

$$r, \varphi = \theta + \frac{2\pi}{\lambda} z \quad \text{and} \quad r, \zeta = z + \frac{\lambda}{2\pi}\theta, \tag{2.9a, b}$$

which allow the reduction of the three-dimensional Lagrangian system

$$\frac{\mathrm{d}r}{\mathrm{d}t} = V_r(r,\theta,z), \quad \frac{\mathrm{d}\theta}{\mathrm{d}t} = \frac{1}{r}V_\theta(r,\theta,z), \quad \frac{\mathrm{d}z}{\mathrm{d}t} = V_z(r,\theta,z). \tag{2.10}$$

to the following equivalent two-dimensional systems:

$$\frac{\mathrm{d}r}{\mathrm{d}t} = V_r(r,\varphi), \quad \frac{\mathrm{d}\varphi}{\mathrm{d}t} = \frac{1}{r}\left[V_\theta(r,\varphi) + \frac{2\pi r}{\lambda}V_z(r,\varphi)\right] \equiv \frac{1}{r}V_\varphi(r,\varphi), \tag{2.11a, b}$$

$$\frac{\mathrm{d}r}{\mathrm{d}t} = V_r(r,\zeta), \quad \frac{\mathrm{d}\zeta}{\mathrm{d}t} = V_z(r,\zeta) + \frac{\lambda}{2\pi r}V_\theta(r,\zeta) \equiv V_\zeta(r,\zeta). \tag{2.12a, b}$$

Starting from relations (2.11)–(2.12) and the continuity equation $\boldsymbol{\nabla}\cdot\boldsymbol{V} = 0$ for the three-dimensional velocity field $\boldsymbol{V}$ formulated in cylindrical coordinates, it is easy to prove that the reduced two-dimensional velocity fields (V_r, V_φ) and (V_r, V_ζ) satisfy the continuity equation formulated in polar cylindrical coordinates

$$\frac{1}{r}\frac{\partial}{\partial r}(r V_r) + \frac{1}{r}\frac{\partial V_\varphi}{\partial \varphi} = 0, \tag{2.13}$$

and axisymmetric cylindrical coordinates

$$\frac{1}{r}\frac{\partial}{\partial r}(r V_r) + \frac{\partial V_\zeta}{\partial \zeta} = 0, \tag{2.14}$$

respectively, using the following identities:

$$\frac{\partial}{\partial \theta} = \frac{\partial}{\partial \varphi} = \frac{\lambda}{2\pi}\frac{\partial}{\partial \zeta} = \frac{\lambda}{2\pi}\frac{\partial}{\partial z}. \tag{2.15}$$

Therefore, projecting the velocity field onto the (r, φ)-coordinate system is equivalent to transforming the flow domain in a translation-invariant annular geometry and considering a transverse section with φ as the azimuthal coordinate. Equivalently, projecting onto the (r, ζ)-coordinate system corresponds to looking at an axisymmetric annular geometry and considering a meridional plane with ζ as the axial coordinate. In other words, given (2.9*a*, *b*), the (r, φ)-plane for $r \in [R_1, R_2]$ and $\varphi \in [0, 2\pi]$ corresponds to a transverse cut at $z = 0$, with $r \in [R_1, R_2]$ and $\theta \in [0, 2\pi]$, while the (r, ζ)-plane for $r \in [R_1, R_2]$ and $\zeta \in [0, \lambda]$ corresponds to a meridional cut at $\theta = 0$, with $r \in [R_1, R_2]$ and $z \in [0, \lambda]$. The two reduced coordinate systems are equivalent as information can be mapped from one to the other using $\varphi = 2\pi\zeta/\lambda$ and $V_\varphi = 2\pi r V_\zeta/\lambda$. Let us use a

general decomposition of the velocity field into a reference flow field $\boldsymbol{V}^{\mathrm{ref}}$ satisfying the heterogeneous boundary conditions and the continuity equation, plus a fluctuating field in the (r, ζ)-coordinate system:

$$V_r(r, \zeta) = v_r(r, \zeta), \quad V_\zeta(r, \zeta) = V_\zeta^{\mathrm{ref}}(r) + v_\zeta(r, \zeta), \tag{2.16}$$

where

$$V_\zeta^{\mathrm{ref}}(r) = V_z^{\mathrm{ref}}(r) + \frac{\lambda}{2\pi r} V_\theta^{\mathrm{ref}}(r). \tag{2.17}$$

This decomposition leads to the following two-dimensional homogeneous kinematics problem satisfied by the velocity field (v_r, v_ζ):

$$\frac{1}{r}\frac{\partial}{\partial r}(r v_r) + \frac{\partial v_\zeta}{\partial \zeta} = 0 \quad \text{with} \quad (v_r, v_\zeta) = (0, 0) \quad \text{at } r = R_1 \text{ and } R_2. \tag{2.18}$$

Equations (2.14) and (2.18) imply that both two-dimensional velocity fields (V_r, V_ζ) and (v_r, v_ζ) are area-preserving; therefore we can introduce a streamfunction

$$\Psi(r, \zeta) = \Psi^{\mathrm{ref}}(r) + \psi(r, \zeta), \tag{2.19}$$

such that

$$v_r(r, \zeta) = \frac{1}{r}\frac{\partial \psi(r, \zeta)}{\partial \zeta}, \quad v_\zeta(r, \zeta) = -\frac{1}{r}\frac{\partial \psi(r, \zeta)}{\partial r}, \tag{2.20a, b}$$

$$V_\zeta^{\mathrm{ref}}(r) = -\frac{1}{r}\frac{\partial \Psi^{\mathrm{ref}}(r)}{\partial r}, \quad \Psi^{\mathrm{ref}}(R_2) = 0, \tag{2.21a, b}$$

with (2.21b) corresponding to the no-slip condition on the fixed outer cylinder.

The velocity approximation is now recast as a streamfunction approximation problem, albeit indirect, since only velocity measurements are available. We seek trial functions for $\psi(r, \zeta)$ that are separable in (r, ζ), periodic in ζ with period λ, and obey the homogeneous boundary conditionsy

$$\forall \zeta, \quad \psi(R_1, \zeta) = \psi(R_2, \zeta) = 0. \tag{2.22}$$

The candidate perturbation streamfunction may take the form

$$\psi(r, \zeta) = \sum_{i=1}^{N} \sum_{k=0}^{M} \left[F_{i,k} \cos\left(\frac{2\pi k}{\lambda}\zeta\right) + G_{i,k} \sin\left(\frac{2\pi k}{\lambda}\zeta\right) \right] T_i(\hat{r}), \tag{2.23}$$

where N and M are the approximation orders in r and ζ, respectively, and k is the wavenumber in the ζ-direction. $\{T_i(\hat{r}), i \in [1, N]\}$ represents a set of orthogonal functions whose dependence on the non-dimensional variable $\hat{r} = r/R_2$ has yet to be determined. $\{(F_{i,k}, G_{i,k}),\ i \in [1, N],\ k \in [0, M]\}$ are the approximation coefficients $(G_{i,0} \equiv 0,\ \forall i)$. The trigonometric functions are orthogonal in the interval $\zeta \in [0, \lambda]$, and they form a complete set as $M \to \infty$.

Combining (2.23) with (2.20) yields

$$v_r(r, \zeta) = \sum_{i=1}^{N} \sum_{k=1}^{M} \left[-F_{i,k} \sin\left(\frac{2\pi k}{\lambda}\zeta\right) + G_{i,k} \cos\left(\frac{2\pi k}{\lambda}\zeta\right) \right] \frac{2\pi k}{\lambda r} T_i(\hat{r}), \tag{2.24}$$

and

$$v_\zeta(r, \zeta) = \sum_{i=1}^{N} \sum_{k=0}^{M} \left[-F_{i,k} \cos\left(\frac{2\pi k}{\lambda}\zeta\right) - G_{i,k} \sin\left(\frac{2\pi k}{\lambda}\zeta\right) \right] \frac{1}{R_2 r} T_i'(\hat{r}), \tag{2.25}$$

where $T_i'(\hat{r})$ is the derivative of $T_i(\hat{r})$ with respect to $\hat{r}$.

The no-slip boundary conditions (2.18) combined with (2.24) and (2.25) for (v_r, v_ζ) require that the functions $T_i(\hat{r})$ satisfy

$$T_i(\eta) = T_i(1) = 0, \quad T_i'(\eta) = T_i'(1) = 0. \tag{2.26}$$

Therefore, the functions $T_i(\hat{r})$ must satisfy a fourth-order differential equation with four homogeneous boundary conditions. A family of orthogonal functions satisfying the boundary conditions (2.26) for the same annular geometry was constructed up to the third order by Chandrasekhar & Elbert (1958). These functions take the form

$$T_i(\hat{r}) = J_1(\alpha_i \hat{r}) + a_i Y_1(\alpha_i \hat{r}) + b_i I_1(\alpha_i \hat{r}) + c_i K_1(\alpha_i \hat{r}) \tag{2.27}$$

where J_1, Y_1, I_1, and K_1 are the first-order Bessel functions of various kinds in Watson's (1944) notation, α_i is the ith root of the characteristic equation

$$\begin{vmatrix} J_1(\alpha_i) & Y_1(\alpha_i) & I_1(\alpha_i) & K_1(\alpha_i) \\ J_1(\alpha_i\eta) & Y_1(\alpha_i\eta) & I_1(\alpha_i\eta) & K_1(\alpha_i\eta) \\ J_0(\alpha_i) & Y_0(\alpha_i) & I_0(\alpha_i) & -K_0(\alpha_i) \\ J_0(\alpha_i\eta) & Y_0(\alpha_i\eta) & I_0(\alpha_i\eta) & -K_0(\alpha_i\eta) \end{vmatrix} = 0, \tag{2.28}$$

which corresponds to the four boundary conditions (2.26), and $(1, a_i, b_i, c_i)$ is the eigenvector associated with the zero eigenvalue of the matrix on the left-hand side of (2.28). The functions $T_i(\hat{r})$ have $(i-1)$ zeros in addition to their zeros on the boundaries. By employing CERN Fortran libraries, the numerical values for $(\alpha_i, a_i, b_i, c_i)$ are computed here for up to $i = 5$ with machine accuracy, so that the four homogeneous boundary conditions (2.26) are satisfied with a maximum residual of 10^{-7}.

2.4. *Choice of a reference flow field*

The reference flow field is introduced so that the fluctuation flow field (v_r, v_ζ) has homogeneous boundary conditions and a complete set of basis functions can be obtained for the approximation of the fluctuation streamfunction ψ. By construction, the use of the fluctuation streamfunction ψ (2.20) and its homogeneous boundary conditions (2.22) forces the average of v_ζ over the flow domain (r, ζ) to cancel out:

$$\begin{aligned} \int_{\zeta=0}^{\lambda} \int_{r=R_1}^{R_2} v_\zeta(r, \zeta) r \, \mathrm{d}r \, \mathrm{d}\zeta &= -\int_{\zeta=0}^{\lambda} \int_{r=R_1}^{R_2} \frac{\partial \psi(r, \zeta)}{\partial r} \, \mathrm{d}r \, \mathrm{d}\zeta \\ &= -\int_{\zeta=0}^{\lambda} [\psi(R_2, \zeta) - \psi(R_1, \zeta)] \, \mathrm{d}\zeta = 0. \end{aligned} \tag{2.29}$$

As mentioned in § 2.2, the velocity measurements indicate that the flow domain average of v_z is zero but that of v_θ is not. In (2.29), since $v_\zeta = v_z + v_\theta \lambda / 2\pi r$ and the average of v_z is zero, the actual average that matters is that of v_θ / r, which, from the data, has a non-negligible value of about 20% of the mean value for V_θ^{CP}/r. Therefore the reference flow field cannot be constituted merely by the Couette–Poiseuille profile and needs an additional term for the θ-component of the composite velocity V_ζ. Furthermore, this additional term should depend only on the radial coordinate, so that it does not induce a undesired radial velocity component, thus inherently satisfying the continuity equation.

An appropriate choice is given by

$$V_\zeta^{\mathrm{ref}}(r) = V_z^{\mathrm{CP}}(r) + \frac{\lambda}{2\pi r} \left[V_\theta^{\mathrm{CP}}(r) + \hat{v}_\theta(r) \right], \tag{2.30}$$

where

$$\hat{v}_\theta(r) = \frac{1}{\lambda}\int_0^\lambda v_\theta(r,\zeta)\,\mathrm{d}\zeta. \tag{2.31}$$

Then, the reference streamfunction becomes

$$\Psi^{\mathrm{ref}}(r) = -\int_{R_2}^{r}\left\{ rV_z^{\mathrm{CP}}(r) + \frac{\lambda}{2\pi}\left[V_\theta^{\mathrm{CP}}(r) + \hat{v}_\theta(r)\right]\right\}\mathrm{d}r. \tag{2.32}$$

Since the measurements of (v_r, v_θ) were not made on the same grid as those for v_z, the construction of the sample space for the composite velocity component v_ζ requires the interpolation or approximation of the two components (v_θ, v_z) onto a common grid. We choose to approximate v_θ onto the v_z-grid using a global approximation function which satisfies the no-slip boundary conditions and allows a non-zero global average (thanks to the terms for $k=0$):

$$v_\theta(r,\zeta) = (r-R_2)(r-R_1)\sum_{i=-N}^{N}\sum_{k=0}^{M}\left\{O_{i,k}\cos\left(\frac{2\pi k}{\lambda}\zeta\right) + P_{i,k}\sin\left(\frac{2\pi k}{\lambda}\zeta\right)\right\}r^i. \tag{2.33}$$

Using $N=2$ and $M=2$ provides an r.m.s. error below the measurement error. Our choice of interpolating v_θ onto the v_z-grid then allows the computation of the additional term $\hat{v}_\theta(r)$ in the reference flow field using (2.31), which leads to

$$\hat{v}_\theta(r) = (r-R_2)(r-R_1)\sum_{i=-N}^{N}\{O_{i,0}r^i\}. \tag{2.34}$$

Equation (2.33) is then evaluated at the grid points where v_z is available, $\hat{v}_\theta(r)$ is calculated analytically, and a data set for the composite velocity v_ζ is constructed using (2.12*b*) and (2.30).

2.5. *Implementation of the discrete least-squares approximation method*

The approximation of the measured radial velocity using (2.24) leaves the coefficients $\{F_{i,0}, i\in[1,N]\}$ of the streamfunction undetermined, while the approximation using (2.25) fixes all the coefficients for the streamfunction. This raises the problem of matching the coefficients shared in (2.24) and (2.25). Since the streamfunction is fully determined by approximating v_ζ, we only use the results from approximating v_ζ and then check the agreement between the radial velocity component derived from this approximation and our measurements for V_r.

The final issue to be resolved for the reconstruction of the streamfunction in (2.23) is the choice of approximation orders, N and M. While only eleven samples are available in the r-direction, 22 velocity samples are available in the ζ-direction. This limits the truncation levels to $N\leqslant 5$ and $M\leqslant 10$ in order to avoid aliasing artefacts. We choose to set $N=5$, but the limit $M=10$ is unrealistic, since the data originating from the transverse sections do not possess a comparable number of samples in the azimuthal direction. A rational method to determine the truncation level M would generally involve extrinsic constraints in addition to limiting the velocity truncation error to levels below the measurement error. Such extrinsic constraints can be introduced by considering the *dynamics* and constitutive equations of the fluid. For example, it is feasible to measure the average mechanical power input and relate it directly to the average viscous dissipation in SHV. Let Φ denote the local viscous dissipation function of the full velocity field of a Newtonian fluid. By using (V_r, V_θ, V_z) expressed

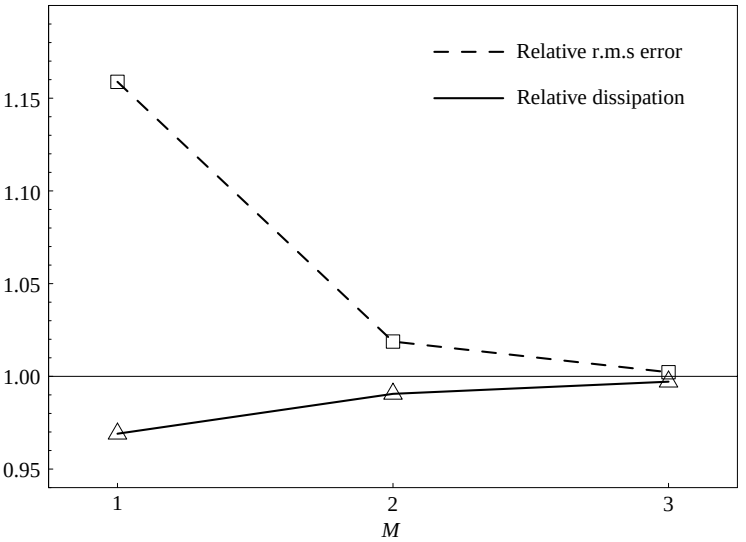

FIGURE 3. Plot for $N = 5$ of the r.m.s. of the difference between the approximated and measured V_ζ normalized by the maximum measured value for V_ζ, and the volume-average dissipation function Φ divided by the asymptotic value using Shank's transform for both quantities, versus the approximation order M in (2.23).

in the (r, ζ)-coordinate system and employing (2.15), Φ takes the form

$$\Phi(r,\zeta) = 2\left[\left(\frac{\partial V_r}{\partial r}\right)^2 + \left(\frac{\lambda}{2\pi r}\frac{\partial V_\theta}{\partial \zeta} + \frac{V_r}{r}\right)^2 + \left(\frac{\partial V_z}{\partial \zeta}\right)^2\right] + \left(\frac{\partial V_r}{\partial \zeta} + \frac{\partial V_z}{\partial r}\right)^2 + \left(\frac{\lambda}{2\pi r}\frac{\partial V_z}{\partial \zeta} + \frac{\partial V_\theta}{\partial \zeta}\right)^2 + \left(\frac{\lambda}{2\pi r}\frac{\partial V_r}{\partial \zeta} + \frac{\partial V_\theta}{\partial r} - \frac{V_\theta}{r}\right)^2, \quad (2.35)$$

where (V_r, V_θ) are the approximated functions according to (2.24) and (2.33), and V_z is extracted from (2.12*b*) using the approximated V_ζ from (2.25) and V_θ. Then, the integral of Φ over the flow field, which can be represented by the area integral over the flow domain $(r, \zeta) \in [R_1, R_2] \times [0, \lambda]$, forms a metric, which can be employed to determine the level of truncation M. Figure 3 shows the convergence of the approximation error for $N = 5$ and M up to 3, in terms of two L_2-norms: the r.m.s. of the difference between the approximated and the measured V_ζ, and the volume-averaged viscous dissipation function, both normalized by their asymptotic value obtained via Shank's transform (17.8% and 19.6 $\mathrm{cm^3\,s^{-2}}$, respectively). For $M = 3$, both the r.m.s. norm and the dissipation norm are less than 1% different from their respective asymptotic values.

The radial velocity component V_r extracted from the streamfunction is then found to differ from the measurements of U by an r.m.s. value of 10%, which is consistent with a general velocity measurement error of 10% for complex flow fields. Therefore, we truncate our approximation scheme at $N = 5$ and $M = 3$, which requires the determination of 35 coefficients for the approximation of the streamfunction Ψ. Although the r.m.s. error between our approximation of V_ζ and the measurements seems a bit large, it can be explained in terms of the error accumulation resulting from data coarseness and Cartesian to cylindrical coordinate conversions. Furthermore, such discrepancies between measurement and approximation become inconsequential

in view of the excellent agreement of the latter with the more accurate numerical simulation of the SHV mode to be discussed in § 3.2.

An alternative reference flow field is provided by the mean velocity profile $\overline{\boldsymbol{V}}(r)$, which is defined in the cylindrical and reduced coordinate systems by

$$\overline{\boldsymbol{V}}(r) \equiv \frac{1}{2\pi\lambda}\int_{z=0}^{\lambda}\int_{\theta=0}^{2\pi}\boldsymbol{V}(r,\theta,z)\,\mathrm{d}\theta\,\mathrm{d}z \equiv \frac{1}{\lambda}\int_{=0}^{\lambda}\boldsymbol{V}(r,\zeta)\,\mathrm{d}\zeta. \tag{2.36}$$

Since there is no net radial flux in or out of the control volume defined by the first integral of (2.36), $\overline{V_r}(r)=0$ by definition. Furthermore, since the other velocity components ($\overline{V_\theta}$ and $\overline{V_z}$ in cylindrical coordinates or $\overline{V_\zeta}$ in the reduced coordinates) only depend on r, $\overline{\boldsymbol{V}}(r)$ inherently satisfies the continuity equation and the helical symmetry (2.1). Also, the mean flow profile obeys *de facto* the boundary conditions, and thus constitutes a valid candidate for the reference flow field. In general, $\overline{\boldsymbol{V}}(r)$ could be obtained either numerically or experimentally. In the present study, the velocity components (V_z on a polar grid and V_θ on a Cartesian grid) were measured with low resolution, which makes the computation of a mean profile for V_ζ unreliable. The choice of the approximation function for the velocity components given in (2.24) and (2.25) compensates for the potential differences between the reference flow field initially chosen by (2.30) and the alternative $\overline{\boldsymbol{V}}(r)$.

In summary, the approximation of the three-dimensional velocity field in the SHV mode is performed in three stages. First, the azimuthal velocity component is approximated using the functional form given in (2.33) that satisfies the boundary conditions and allows a non-zero flow domain average. This makes it possible to calculate $\hat{v}_\theta(r)$ via (2.34) and the reference flow field V_ζ^{ref} via (2.30), thus enabling the construction of a new sample space for v_ζ. Second, these sample values of v_ζ are approximated using (2.25), from which is derived the analytical form of the streamfunction ψ by evaluating the coefficients in (2.23). The radial velocity component V_r can then be computed using (2.24) and validated against our measurements, and this completes the approximation of the three-dimensional velocity field. Third, the two norms, the r.m.s. difference with the data and the dissipative energy, are calculated as functions of the truncation levels for the velocity approximations and checked for convergence. Ultimately, the approximation produces an analytical velocity field that exactly satisfies the boundary conditions and the continuity equation, exactly matches the experimental flow rate measurement, and is consistent with our MRI measurements within the experimental error (10%) of the velocimetry technique used here.

3. Flow topology of the SHV mode

In this section, we analyse the results from the numerical approximation of the streamfunction of the SHV mode by constructing the streamline portrait of the flow. We subsequently provide support for the proposed streamline portrait in three ways: (i) by invoking topological constraints and structural stability criteria, (ii) by listing corroborative experimental and numerical evidence, and finally, (iii) by comparing the topology of the SHV mode and the most probable PTV mode.

3.1. *Streamline portrait and flow topology*

The determination of the streamfunction of the SHV mode allows the construction of a streamline portrait of the flow, or flow skeleton (cf. MacKay 1994). This map contains the critical points and the limiting fluid particle trajectories characterizing the flow. The SHV flow skeleton is presented in the (r,φ)-plane (or transverse section) in

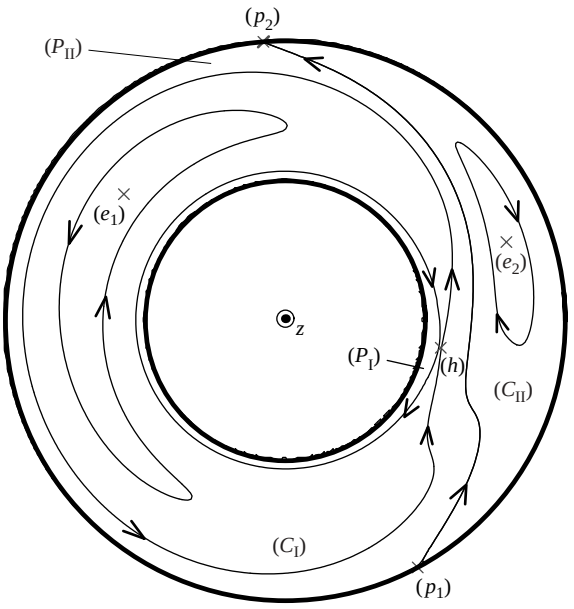

FIGURE 4. Two-dimensional flow skeleton in SHV flow in the (r, φ)-plane. The arrows give the direction of the fluid particle trajectories. (e), (h), and (p) denote elliptic, hyperbolic, and parabolic points, respectively. (C_I) and (C_{II}) label the vortices rotating in the same and opposite direction as the inner cylinder, respectively, while (P_I) and (P_{II}) mark the annular regions containing fibre-like periodic orbits. The streamline through (h) is a separatrix. The three-dimensional flow skeleton can be reconstructed by simultaneous translation along z and rotation around z of this two-dimensional flow skeleton.

figure 4 and in the (r, ζ)-plane (or meridional section) in figure 5. These sections of the three-dimensional streamfunction essentially correspond to transverse and meridional cuts of the three-dimensional streamtubes, and are equivalent to the mapping of three-dimensional trajectories of fluid particles into the reduced coordinate systems. Mathematically speaking (Abraham *et al.* 1988, section 3.4), fluid trajectories are the *fibres* of the flow domain, which constitute a local *vector bundle*. Figures 4 and 5 are two *projections* of the vector bundle. Two recirculating cells are clearly delineated, each with an elliptic point in its centre, corresponding to the two counter-rotating helical vortices in the double helix topology. In the following discussion and in the rest of the article, we shall use the following terminology to distinguish between the two vortices. By considering the transverse section of the streamfunction presented in figure 4, the rotation of the inner cylinder twists the fluid counter-clockwise, and the vortex rotating in the same direction as the inner cylinder is labelled co-rotating, while the other is called counter-rotating.

The counter-rotating cell is labelled (C_I), enclosing the elliptic point (e_1), while the co-rotating cell is denoted (C_{II}) and encloses the elliptic point (e_2). The counter-rotating vortex in (C_I) is much larger than the co-rotating vortex in (C_{II}) and this can be explained by conservation of angular momentum in the fluid, as will be shown in § 3.3. The (C_I) cells form a cat's eye pattern in the ζ-direction, with a hyperbolic point (h) between repeating cells. The cell (C_{II}) is bounded by two parabolic points, denoted (p_1) and (p_2), on the outer cylinder wall. The two remaining flow regions contain periodic orbits: (P_I) is located near the inner cylinder, the other, (P_{II}), lies between the cells (C_I) and (C_{II}). Although it appears in figure 5 that the region (P_I)

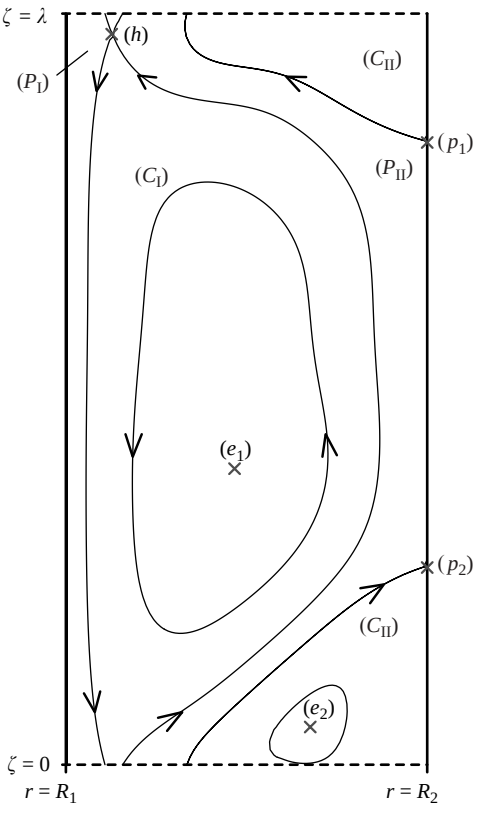

FIGURE 5. Two-dimensional flow skeleton in SHV flow in the (r, ζ)-plane. The meaning of arrows and all nomenclature is consistent with figure 4.

corresponds to a negative axial flow, it should be recalled that the view corresponds to the reduced coordinates (r, ζ). Therefore, a negative displacement in the ζ-direction ($\Delta\zeta < 0$) does not necessarily correspond to a negative displacement in the z-direction, as it originates from the combination of the displacement in the θ-direction $\Delta\theta$ and in the z-direction Δz, such that $\Delta z + \lambda\Delta\theta/2\pi < 0$. In the present case, since the inner cylinder rotation is in the negative θ-direction, a negative displacement in the ζ-direction in (P_I) is likely to result from a negative displacement in the θ-direction overcoming the displacement in the z-direction, which appears more clearly in figure 4. The representation of geometric objects in the reduced coordinates (r, φ) or (r, ζ), as opposed to the (r, z) or (r, θ) coordinates, is further clarified in the next paragraph by relating the three-dimensional SHV structure to the two-dimensional cuts.

The three-dimensional flow structure of the SHV mode is shown in figure 6, where a few iso-contours of the streamfunction representing streamtubes are plotted for a flow domain spanning two axial wavelengths. Meridional and transverse sections of the streamfunction are also represented in order to elucidate the topology of the streamfunction. Figure 6(a) focuses on the two counter-rotating helical vortices, while figure 6(b) shows the three-dimensional structure of the cat's eye pattern that encloses the cell (C_I). Since the flow is steady, the streamlines and fluid particle trajectories are identical. Let us consider a particle trajectory on one of the streamtubes shown in figure 6(a). The trajectory projected onto the (r, φ)-plane corresponds to mapping the three-dimensional trajectory along the streamtube to the top (or bottom) transverse

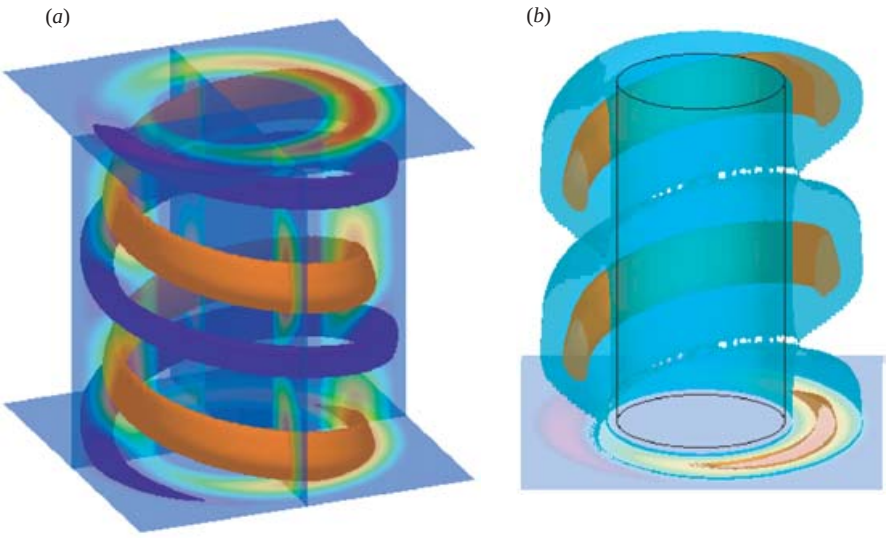

FIGURE 6. Three-dimensional plots of the approximated streamfunction Ψ in SHV flow for two axial wavelengths. (*a*) The two counter-rotating helical vortices are outlined using three-dimensional contour plots for two values of Ψ, while meridional and transverse sections show the spatial structure of the flow. (*b*) The cell (C_{I}) is enclosed in the two-dimensional cat's eye manifold, and one two-dimensional manifold of periodic orbits corresponding to the counter-rotating vortex.

plane in figure 6(*a*). Similarly, the trajectory projected onto the (r, ζ)-plane corresponds to mapping the three-dimensional trajectory along the streamtube to one of the two meridional planes in figure 6(*a*).

It is useful to recast the description of the SHV streamline portrait in terms of dynamical systems nomenclature. By comparing the three-dimensional plot in figure 6 with the projections depicted in figures 4 and 5, it becomes clear that the boundary of cell (C_{II}) is a two-dimensional manifold heteroclinic to two invariant one-dimensional manifolds passing through points (p_1) and (p_2). The two one-dimensional manifolds form two helices on the outer cylinder surface. Similar topology characterizes the boundary of cell (C_{I}) depicted in figure 6(*b*), which is a two-dimensional manifold homoclinic to the one-dimensional manifold (also a helix) passing through point (h).

3.2. *Corroborative evidence for the proposed SHV streamline portrait*

Based on global geometric constraints, we can show that the streamline portrait in figure 6 obtained from our analytical data approximation for the SHV mode is 'realistic'. The simplest topology constraint is based on the *Euler number* ξ of the flow. As explained by Jana *et al.* (1994), the Euler number of a surface is defined as the sum of the *Poincaré indices* of the critical points on the surface (Abraham *et al.* 1988). The Poincaré index of a hyperbolic point is -1, of a parabolic point is $-\frac{1}{2}$, and of an elliptic point is 1. The annular geometry of the TCP system is imbedded in a one-fold torus (genus $\gamma = 1$), and since $\xi = 2 - 2\gamma$, the Euler number ξ is 0. Therefore the topological invariance relation for TCP is

$$N_{\mathrm{E}} - \left(N_{\mathrm{H}} + \tfrac{1}{2}N_{\mathrm{P}}\right) = \xi = 0, \tag{3.1}$$

where N_{E} is the number of elliptic points, N_{H} is the number of hyperbolic points, and N_{P} is the number of parabolic points. Relation (3.1) in itself does not guarantee

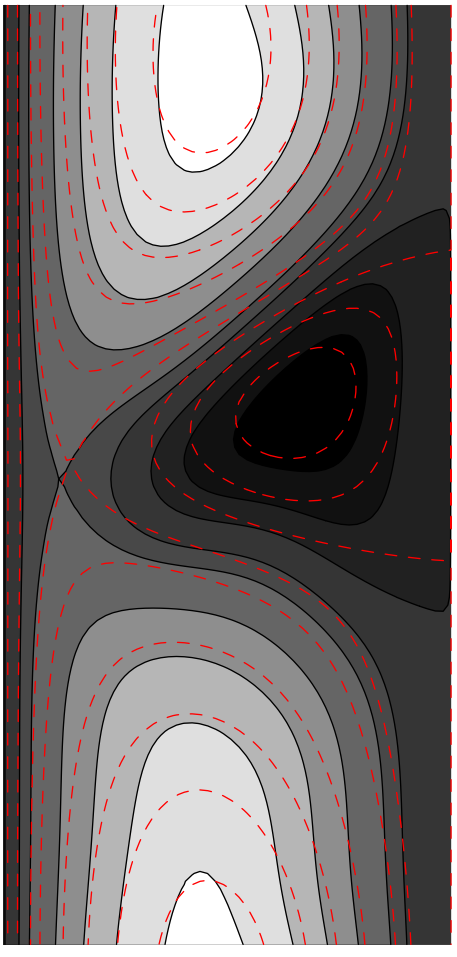

FIGURE 7. Comparison of SHV flow streamlines in the (r, ζ)-plane obtained via the MRI reconstruction (solid contours) with numerical simulation results (dashed lines).

the existence of a flow but it is merely a way to check for topological consistency. Quite obviously, the SHV streamline portrait proposed in figure 5 satisfies (3.1) with $N_E = 2$, $N_H = 1$, and $N_P = 2$.

We can also validate the approximated SHV velocity field by pursuing the idea that the kinematics of a physically realizable flow (like the SHV mode) is related to its stability. Rather than referring to the stability of the 'ideal' SHV flow to infinitesimal perturbations to the flow, we focus on the structural stability of the SHV mode to infinitesimal changes to the geometry and boundary conditions in the TCP system. A structurally stable system is defined as a system that does not change in the qualitative character of its solutions under infinitesimal changes in the governing equations, which includes geometrical and physical parameters of the cavity, fluid properties, and boundary conditions (Drazin & Reid 1981). It is easy to understand the motivation behind the removal of ideal conditions because end effects and forcing inhomogeneities are inherently present in a typical TCP apparatus. The SHV flow depicted in figures 4–6 is *structurally stable* according to theorem (3.2) of Ma & Wang (2001). Indeed, their conditions for the structural stability of divergence-free vector fields that

satisfy Dirichlet boundary conditions (no slip at the walls) are met: (i) the approximated velocity field is sufficiently regular, (ii) the hyperbolic points are self-connected (as shown in figure 4, (h) is connected to itself), and (iii) a parabolic point on the boundary is connected to another parabolic point on the same boundary ((p_1) is connected to (p_2), and both are located on the outer cylinder). Basically, by verifying that the flow structure is structurally stable, we are further corroborating the fidelity of the reconstruction of the SHV velocity field from the coarse MRI measurements.

More direct evidence for the validity of the streamline portrait depicted in figure 6 can be gleaned from experimental observations of the SHV mode using flake visualization (cf. Lueptow *et al.* 1992). Indeed, the two parabolic points located on the outer cylinder in figure 5 are connected with stable and unstable manifolds, which correspond to inflow and outflow regions separating the counter-rotating cells that become visible as lines limiting the two vortices when the flow is observed through the outer cylinder. Moreover, the presence of the annular region (P_{II}) delineated in figure 5 is corroborated by dye injection experiments conducted by the present authors in the same apparatus used in the MRI study reported here (cf. Raguin, Shannon & Georgiadis 2001).

Finally, the strongest support for the SHV mode, as reconstructed here, was obtained by the authors' research group using direct numerical simulation. Starting with the reconstructed SHV field as an initial guess, the 'ideal' SHV solution (which satisfies the Navier–Stokes equations) was obtained numerically using a three-dimensional Lattice–Boltzman code with periodic conditions over the span of one axial wavelength fixed at the measured value of $\lambda = 20\,\mathrm{mm}$ (Holdych 2003). A steady SHV mode was obtained for $Re = 11.14$ and $Ta^{1/2} = 170$ using a uniform Cartesian grid with spatial resolution 0.1667 mm, which corresponds to $\lambda/120$. The numerical solution converges to a steady flow field which exhibits a helical symmetry, satisfying (2.1) for each velocity component (V_r, V_θ, V_z) with an r.m.s. error of 0.080%, 0.022%, and 0.071%, respectively (the r.m.s. values are normalized by the maximum value for each velocity component). The satisfaction of both the continuity equation and the helical symmetry relation similarly allows the computation of a streamfunction in the reduced coodinates (r, ζ). As figure 7 demonstrates, the experimentally approximated velocity field and the numerically determined velocity field agree in terms of all important flow skeleton aspects. In fact, the numerical solution obtained in the vicinity of the (Re, Ta) parameters, for which the SHV mode was reconstructed here, exhibits the same streamline portrait characteristics: two counter-rotating vortices, the larger one in a cat's eye pattern and the other enclosed in a cell bounded to the outer cylinder wall. Most importantly, the two flow fields differ by an r.m.s. error of less than 10.5%, 10%, and 11% in the radial, azimuthal, and axial velocity components, respectively, and by 7% in the streamfunction, all of which are consistent with the 10% experimental error.

3.3. *The SHV flow structure in relation to the PTV mode(s)*

As mentioned in § 1.2, the PTV mode constitutes the neighbouring state of the SHV mode; therefore, it is instructive to compare their topologies. Simplistically, the flow structure of the PTV mode can be described by translating the axisymmetric TC flow structure shown in figure 8(a) along the z-axis with constant speed (see e.g. Bühler & Polifke 1990). However, since the heteroclinic orbit connecting the two parabolic points would now span the annulus from one cylinder to the other, this flow structure is *structurally unstable*, according to theorem (3.2) of Ma & Wang (2001), and the analysis of the Taylor vortices by Benjamin (1978a,b) and Ma & Wang (2000). To

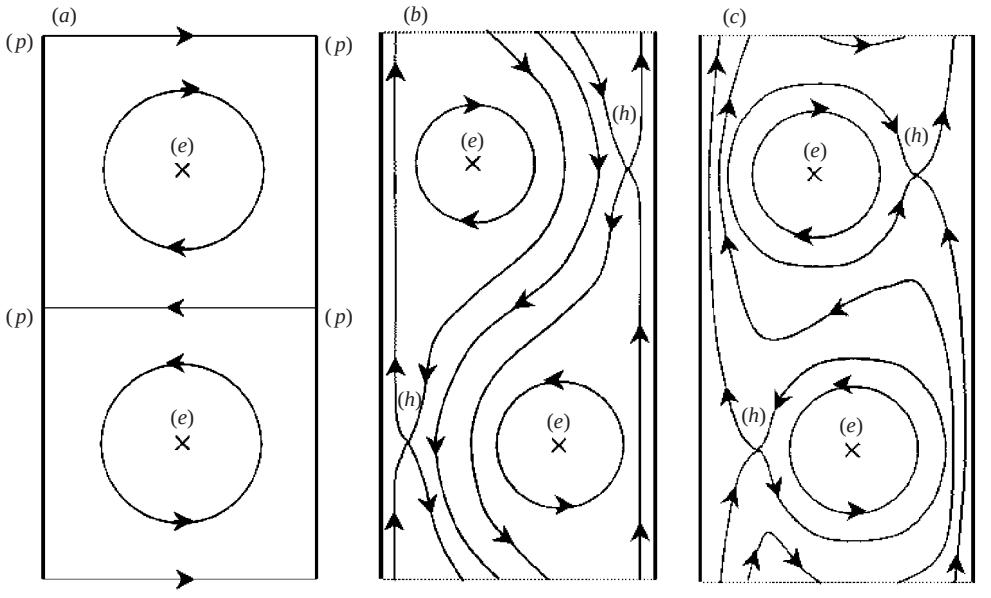

FIGURE 8. Streamline portrait of TC flow and two types of PTV in the (r, ζ')-plane for one axial wavelength, with $\zeta' = z - U_d t$ where U_d is the axial drift velocity of the travelling vortices. (e) denotes elliptic points, (h) hyperbolic points, and (p) parabolic points. (a) TC flow (zero mean axial flow, and $U_d = 0$); (b) PTV(I): PTV with meandering back-flow; (c) PTV(II): PTV with meandering forward-flow.

obtain a realistic flow structure, Haim & Pismen (1994) used the eigenfunctions for the PTV mode obtained numerically by Ng & Turner (1982) for various values of Re and η, and computed the streamline fields for different values of the amplitude of the eigenfunction. They found two types of PTV flows, the first (denoted PTV(I)) with a meandering flow in the direction opposite to the imposed axial through-flow for low values of the eigenfunction amplitude, and the second (labelled PTV(II)) with a meandering flow co-current with the mean flow for large values of the amplitude. Starting from the streamline plots displayed by Haim & Pismen (1994), we constructed the streamline portraits of these two candidate PTV modes and they are shown in figures 8(b) and 8(c). The PTV flow corresponds to translating the portraits along the positive z-axis with the propagating vortex velocity U_d. An increase in the amplitude of the eigenfunction, i.e. of the disturbance relative to CP flow, is consistent with an increase in vortical strength, i.e. an increase of Ta.

Both streamline portraits shown in figures 8(b) and 8(c) satisfy the topological invariance relation given by (3.1), as both possess $N_E = 2$ elliptic points, $N_H = 2$ hyperbolic points, and $N_P = 0$ parabolic points. They also satisfy the conditions for structural stability determined by Ma & Wang (2001), since the hyperbolic points are self-connected. The occurrence of the PTV(II) mode is not as likely as that of the PTV(I) mode because the former requires a larger amplitude of the perturbation eigenfunction, which would further imply that the counter-rotating vortices travel more slowly than the mean axial velocity U (since the meandering forward flow induces a positive flux in the axial direction). Vortices moving slower than the mean flow have only been observed by Giordano *et al.* (1998), but their experimental set-up was similar to that of Bühler & Polifke (1990) in terms of the absence of flow-straighteners at the entrance of the annular region. Moreover, Giordano *et al.* (1998)

used very low axial through-flows with $Re < 1.067$, which, combined with non-negligible inlet flow swirl, is likely to lower the propagation speed U_d of the PTV. In all studies involving the stability analysis of TCP flow (e.g. Takeuchi & Jankowski 1981; Ng & Turner 1982), and most experimental studies of TCP for modest values of Re (< 100) (e.g. Snyder 1962; Lueptow *et al.* 1992; Moser *et al.* 2000*c*; Raguin *et al.* 2001), the drift velocity of the PTV is larger than U, and in most cases approximately $U_d = 1.2U$, which means that the meandering streamlines have negative axial velocity in the reference frame travelling with the PTV. Wereley & Lueptow (1999) also reported the presence of meandering streams, as they performed velocity measurements using PIV in their study of the PTV flow. Furthermore, the existence of such meandering flows was invoked by Raguin *et al.* (2001) in their analogy to the wave propagation in a dispersive media to account for the observation that $U_d > U$ in their dye injection experiments. In conclusion, both theoretical and experimental evidence suggests that the PTV flow portrait resembles the mode PTV(I) given in figure 8(*b*).

The SHV flow topology proposed by Bühler & Polifke (1990) can be obtained by rotating the meridional section in figure 8(*a*) according to the transformation (2.1), which again produces a structurally unstable flow topology (Ma & Wang 2000). In contrast, the SHV flow structure proposed here is topologically close to the prevailing PTV(I) mode given in figure 8(*b*), and they share the flow skeleton complexity as measured by the number and nature of cells and singular points. As the PTV mode is replaced by the SHV mode, the twin counter-rotating toroidal vortices in PTV(I) give rise to the two asymmetric helical counter-rotating vortices depicted in figures 4–6. Intuitively, the rotation of the inner cylinder drives the counter-rotating vortex in (C_I) and consequently makes it larger than the co-rotating vortex in (C_{II}). This asymmetry is justified if we consider the bulk flow to be Eulerian (inviscid approximation) and assume that the viscous effects are limited to the regions close to the walls. Conservation of angular momentum in the bulk flow driven by the inner cylinder requires that the counter-rotating vortex be larger than the co-rotating vortex. This is an important consequence of the transition from the axisymmetric flow structure of the PTV mode to the helical symmetry of the SHV mode. Since the SHV mode has not been extensively studied, no other experimental observation of this asymmetry in the vortex sizes is available in the literature, to the authors' knowledge. However, the numerical simulations performed by Holdych (2003) and depicted in figure 7 do corroborate our finding of a significant size difference between the two counter-rotating vortices.

A better way to compare the strength of the counter-rotating vortices in the SHV mode is to plot the streamfunction $\psi(r, \zeta)$ corresponding to the perturbation velocity field (v_r, v_ζ) in (2.19), instead of the complete streamfunction $\Psi(r, \zeta)$. In figure 9(*a*) $\psi(r, \zeta)$ is represented for one wavelength, while figure 10 shows ψ in a transverse section as a function of (r, φ), which is consistent with the measured velocity field shown in figure 2. Clearly, the two vortices are not of the same size and strength as the counter-rotating vortex in figure 10, i.e. the one shown with the light shades of grey (positive values of ψ), is about 1.9 times larger than the co-rotating vortex in the dark shades of grey (negative values of ψ) at $r = (R_1 + R_2)/2$. Note that the parabolic points on the outer cylinder are diagonally symmetric in figure 10, and equidistant in the meridional plane depicted in figure 9, while the symmetry is broken for the parabolic points on the inner cylinder. This confirms that the inner cylinder rotation combined with the helical symmetry is responsible for the creation of asymmetry between the two counter-rotating vortices when the flow transitions from the PTV mode to the SHV mode.

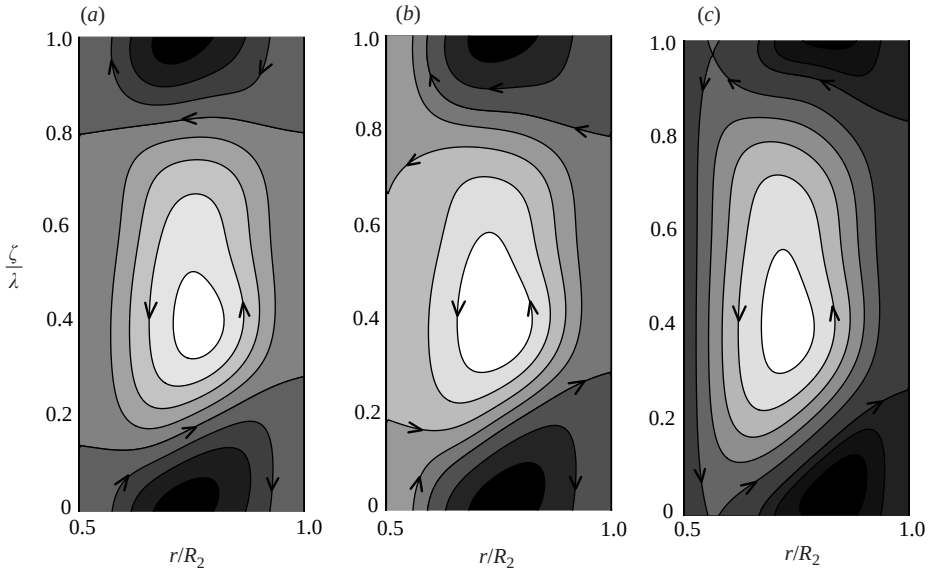

FIGURE 9. Two-dimensional streamlines of (*a*) the perturbation to the reference velocity field, given by (2.23); (*b*) the perturbation to CP flow, given by the sum of (2.23) and the streamfunction due to (2.31); and (*c*) the full SHV velocity field, given by (2.19), in the (r, ζ)-plane with r and ζ scaled with R_2 and λ, respectively. The vortex marked by the dark shades of grey is the counter-rotating vortex, while the one in the light shades of grey is the co-rotating vortex following the same nomenclature as used for figure 4. Separating streamlines connect the inner to the outer cylinder and the reverse, as indicated by arrows.

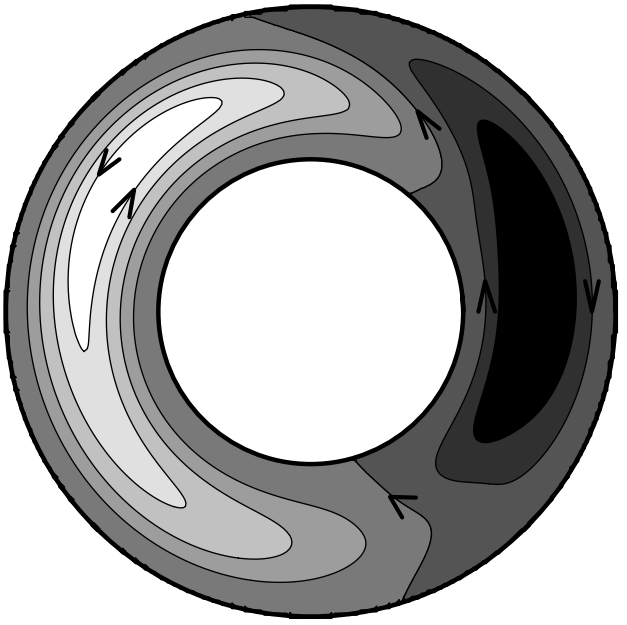

FIGURE 10. Two-dimensional streamlines of the perturbation to the CP streamfunction for SHV flow, given by (2.23), in the (r, φ)-plane. The vortex rotation convention is the same as in figure 9.

Figures 9(*a*)–9(*c*) show the transition in terms of streamfunction fields, from the perturbative velocity field with zero average (v_r, v_ζ) in (*a*), to the velocity field departure from the CP profile in (*b*), to the full SHV velocity field in (*c*). In figure 9(*b*), there is no connecting streamline between the inner and outer cylinder, as both vortices are enclosed in a cell connected to each cylinder. Finally, in figure 9(*c*), the cell containing the large counter-rotating vortex is detached from the inner cylinder, while the smaller cell is still connected to the outer cylinder.

4. Global description of SHV flow

4.1. *Integrability of the SHV flow*

In this section, we apply the analytical tools developed by Mezic & Wiggins (1994) for three-dimensional fluid flows with symmetry to prove that the SHV mode is integrable. Since these tools only require that the velocity field be kinematically admissible, i.e. that the continuity equation and the boundary conditions are satisfied, they apply both to the approximated SHV flow field and to the 'ideal' SHV flow field, which additionally satisfies the incompressible Navier–Stokes equations.

The three-dimensional autonomous Lagrangian system (2.10) is a volume-preserving system of ordinary differential equations, since the velocity field is divergence-free. Furthermore, the velocity field admits a one-parameter volume-preserving spatial symmetry group G defined in cylindrical coordinates by the 'screw' transformation:

$$\forall \boldsymbol{x} = (r, \theta, z) \in S \subset \mathbb{R}^3, \quad \forall \alpha \in [0, \lambda], \quad \boldsymbol{g}(\boldsymbol{x}; \alpha) = \left(r, \theta - \frac{2\pi}{\lambda}\alpha, z + \alpha \right), \tag{4.1}$$

with the following law of composition $\phi(\alpha, \beta)$:

$$\forall \alpha, \beta \in [0, \lambda], \quad \boldsymbol{g}(\boldsymbol{g}(\boldsymbol{x}; \alpha); \beta) = \boldsymbol{g}(\boldsymbol{x}; \phi(\alpha, \beta)), \quad \phi(\alpha, \beta) = \alpha + \beta. \tag{4.2}$$

It is straightforward to show that the family of mappings G defined by (4.1) and (4.2) acting on S forms a one-parameter Lie group with infinitesimal generator given by the vector field $\boldsymbol{w} = (0, -2\pi/\lambda, 1)$. Theorem 2.2 from Mezic & Wiggins (1994) then guarantees that there exists a local change of variables $(r, \theta, z) \longmapsto (\rho, \zeta, \kappa)$ such that the system (2.10) becomes

$$\frac{\mathrm{d}\rho}{\mathrm{d}t} = \frac{\partial H(\rho, \zeta)}{\partial \zeta}, \quad \frac{\mathrm{d}\zeta}{\mathrm{d}t} = -\frac{\partial H(\rho, \zeta)}{\partial \rho}, \quad \frac{\mathrm{d}\kappa}{\mathrm{d}t} = k_3(\rho, \zeta), \tag{4.3a, b, c}$$

where H is a first integral, or Hamiltonian, i.e. a quantity that is preserved by the flow. In the SHV flow, the appropriate change of variables is

$$\rho = \frac{r^2}{2}, \quad \zeta = z + \frac{\lambda}{2\pi}\theta, \quad \kappa = z, \tag{4.4a, b, c}$$

hence $k_3(\rho, \zeta) = V_z(\sqrt{2\rho}, \zeta)$, and the Hamiltonian of the system is related to the streamfunction defined in § 2.2, as follows:

$$H(\rho, \zeta) = \Psi(\sqrt{2\rho}, \zeta). \tag{4.5}$$

We may note in passing that, unlike in the examples cited by Mezic & Wiggins (1994), the infinitesimal generator that defines the symmetry for the SHV mode is not identical to the vorticity of the velocity field. The relationships (4.3*a–c*) indicate that the problem can be decomposed into two velocity components which form a canonical one-degree-of-freedom Hamiltonian system (4.3*a*, *b*), and a third non-zero velocity component (4.3*c*), which depends on the first two variables (ρ, ζ). This confirms that the SHV velocity field is integrable.

4.2. *Qualitative study of scalar transport in the SHV mode*

The coordinates (ρ, ζ) are functionally independent invariants of the 'screw' transformation G given by equation (4.1). The continuous symmetry (2.1) has been used to reduce the three-dimensional SHV flow in three-dimensional space to a three-dimensional flow on the two-manifold (ρ, ζ), which now constitutes the reduced phase space. Casting the problem in this form justifies the use of terminology and methodology of dynamical systems theory (cf. Wiggins 1992). For example, since the infinitesimal generator and velocity field are not everywhere collinear, the SHV flow can be partitioned into a finite number of cells. Each cell is then fibred either into tori, as evidenced by the presence of (C_{I}) and (C_{II}), or into annula $((P_{\mathrm{I}})$ and $(P_{\mathrm{II}}))$, as theorem 4.1 in Mezic & Wiggins (1994) implies. This can be verified by referring to figures 4–6.

In analogy with flow fields containing similar features (Ottino 1989), it is expected that the phase portrait of SHV described above goes through certain qualitative changes when the flow is perturbed. Under small perturbations, say with a perturbation field that itself is Hamiltonian, it is possible for the Hamiltonian system (4.3*a*, *b*) to become non-integrable which is a necessary condition for chaotic behaviour. In fact, flows involving interacting coaxial vortex rings have been shown to be non-integrable (cf. Bagrets & Bagrets 1997). The third component of the equation system (4.3*c*) may additionally be perturbed, which gives the SHV mode an extra degree of freedom to study potential chaotic behaviour in three dimensions (cf. Raguin 2004).

Since the postulated perturbation field is Hamiltonian, the KAM theorem applies, and therefore most of the invariant irrational helical vortices in (C_{I}) and (C_{II}) shown in figure 6 are conserved in the perturbed SHV flow. These helical KAM tubes are invariant surfaces and therefore correspond to zero geometric flux (according to the terminology from MacKay 1994), or equivalently, to a mixing barrier between the vortices (C_{I}) and (C_{II}). Between these KAM surfaces, one expects the potential establishment of chaotic orbits when the SHV is perturbed. For example, the unstable manifold through (p_1) would not coincide with the stable manifold through (p_2). The consequence of the formation of this heteroclinic tangle (Wiggins 1992) would be the enhancing of mixing, or interchange of a passive scalar, between the vortices (C_{I}) and (C_{II}) of the unperturbed SHV flow. This geometric argument supports the prediction that mixing across the counter-rotating cells is minimal for the SHV mode relative to certain perturbed modes. We are not pursuing the quantification of passive scalar transport here; instead we conclude our investigation of the global properties of perturbed SHV states by focusing on viscous dissipation.

4.3. *Viscous dissipation in the SHV mode*

We start by adding a velocity perturbation $\boldsymbol{u} = (u_r, u_\theta, u_z)$ to a reference flow field $\boldsymbol{V} = (V_r, V_\theta, V_z)$ defined in an annular geometry occupied by an incompressible fluid. The flow is driven by a mean axial pressure gradient denoted by P. All quantities are rendered dimensionless by scaling lengths with $d = R_2 - R_1$, velocities with ν/d, time with d^2/ν, and the pressure gradient with ν^2/d^3. Following Joseph (1976) and in the spirit of (2.36), we define the average of a quantity f over a cylinder of radius r and infinite length, denoted with an overbar, as follows:

$$\overline{f}(r, t) \equiv \lim_{L\to\infty} \left[\frac{1}{2L} \int_{-L}^{L} \frac{1}{2\pi} \int_{0}^{2\pi} f(r, \theta, z, t)\, \mathrm{d}\theta\, \mathrm{d}z \right], \tag{4.6}$$

while the spatial average over the whole annulus of a physical quantity f is denoted with brackets, as follows:

$$\langle f \rangle \equiv \langle \overline{f} \rangle \equiv \frac{2}{R_2^2 - R_1^2} \int_{R_1}^{R_2} \overline{f}(r, t) r \, \mathrm{d}r. \tag{4.7}$$

This study is limited to a perturbative velocity field with zero cylindrical average, i.e. $\overline{\boldsymbol{u}} = \boldsymbol{0}$, driven by a constant P. The continuity equation combined with the boundary conditions for the annular geometry gives $\langle \overline{V_r} \rangle = 0$. Then, starting from the incompressible Navier–Stokes equations, the spatial average of the total kinetic energy equation over an annulus with an inner cylinder rotating with angular velocity Ω is given by

$$\frac{1}{2}\frac{\mathrm{d}}{\mathrm{d}t}\langle |\overline{V_\theta}|^2 + |\overline{V_z}|^2 + |\boldsymbol{u}|^2 \rangle = 2Re\, P + \tfrac{1}{2} Ta\, T - \left\langle |\nabla \boldsymbol{u}|^2 + \left| \frac{\partial \overline{V_\theta}}{\partial r} \right|^2 + \left| \frac{\partial \overline{V_z}}{\partial r} \right|^2 + \frac{\overline{V_\theta}^2}{r^2} \right\rangle, \tag{4.8}$$

where T is the dimensionless torque imposed on the fluid by the rotating inner cylinder defined by

$$T = -\frac{1}{\Omega} \frac{\partial \overline{V_\theta}}{\partial r}(R_1). \tag{4.9}$$

Equation (4.8) is a modification of the expression derived by Joseph (1976) for annular Poiseuille flow with the addition of a shaft work term (second term of the right-hand side). It merely expresses the fact that the total kinetic energy production is balanced by the work of the axial pressure gradient and the work of the torque of the inner cylinder from which the total viscous dissipation must be subtracted.

Let us consider a perturbation $\boldsymbol{u}$ to a steady reference velocity field $\boldsymbol{V}$ (e.g. CP or SHV), so that the first two terms of the left-hand side of (4.8) are zero. Equivalently, the Hamiltonian H, or correspondingly the streamfunction Ψ, can be perturbed, leading to the functional form for $\boldsymbol{u}$. Since the Hamiltonian only fixes the two-dimensional velocity field (u_r, u_ζ) as seen in (4.3a, b), the third component of the Hamiltonian system (4.3c) can be independently perturbed, as long as this additional perturbation satisfies $\overline{u_z} = 0$. Such disturbances are encountered experimentally as convective instabilities when the reference stationary velocity field is CP flow, as well as when the reference field is the SHV mode, as Moser *et al.* (2001*b*) reported when investigating the breakup of the SHV mode as the axial Reynolds number is increased. Indeed, the cinematographic image sequences obtained via MRI revealed convective instabilities propagating along the helical vortices. For this type of disturbance, the average kinetic energy equation (4.8) reduces to

$$\frac{1}{2}\frac{\mathrm{d}}{\mathrm{d}t}\langle |\boldsymbol{u}|^2 \rangle + \langle |\nabla \boldsymbol{u}|^2 \rangle + \left\langle \left| \frac{\partial \overline{V_\theta}}{\partial r} \right|^2 + \left| \frac{\partial \overline{V_z}}{\partial r} \right|^2 + \frac{\overline{V_\theta}^2}{r^2} \right\rangle = 2Re\, P + \tfrac{1}{2}\, Ta\, T, \tag{4.10}$$

which states that the mechanical energy input (right-hand side) balances the sum of the change in mean kinetic energy, the mean viscous dissipation of the fluctuation field and the mean viscous dissipation of the reference field (left-hand side).

The energy balance equation (4.10) can be further simplified if the fluctuation field has stationary kinetic energy. Taking the temporal average of (4.10) eliminates the fluctuation kinetic energy term (first term on the left-hand side). Consequently, the averaged-over-time equation (4.10) applied to a reference flow field identified with SHV implies that the SHV mode is associated with a minimum in viscous dissipation. Any SHV fluctuation will result in the addition of a positive definite viscous dissipation

term (second term on the left-hand side) and in the corresponding increase of the mechanical energy input required to sustain the flow. The optimality of the SHV mode in terms of minimal mechanical energy input is of course contingent upon introducing perturbations with zero cylindrical averages and stationary average kinetic energy. We note in closing that the asymptotic behaviour of the dissipation norm of equation (2.35) shown in figure 3 is consistent with the existence of the minimum viscous dissipation implied by (4.10).

5. Conclusions

Our central goal was to reconstruct the stationary helical vortex (SHV) mode, a complex duct flow field observed in the Taylor–Couette–Poiseuille system, starting from relatively coarse velocity measurements with non-uniform resolution on a finite number of cross-sections, and to study its kinematics. The velocity measurements were obtained with 10% error by tracking a grid of transient material lines tagged in water with magnetic resonance imaging (MRI). Exploiting the helical symmetry of the SHV mode to its fullest, we achieved our goal by constructing a complete set of orthogonal basis functions in the two-dimensional reduced coordinate system (r, ζ) that are kinematically admissible (incompressible flow, no-slip boundary conditions). The velocity field for the SHV mode was decomposed into a reference flow field profile that accounts for the average properties of the velocity field and an additional velocity field $\boldsymbol{v}$. The complete set of basis functions was used to find an analytical approximation for the streamfunction corresponding to $\boldsymbol{v}$ in terms of a series expansion. The series converged in L_2, and it was truncated according to the convergence of a discrete least-squares error with respect to the point-wise MRI velocity measurements and a volume-averaged viscous dissipation function. Methodologically, our goal was achieved because the SHV mode possesses a continuous volume-preserving symmetry, and we managed to project the approximation onto the space of divergence-free functions that satisfy the appropriate boundary conditions. This work serves to demonstrate the potential of supplementing MRI measurements with appropriate *a priori* fluid mechanical constraints, an idea which has profound implications for reducing the acquisition time for complex cellular flows (cf. Raguin & Georgiadis 2004*a*). The reconstruction of the SHV mode presented here is independent of fluid dynamics constraints, and therefore can be applied to experimental data obtained from the full-field optical imaging of other deformable media acquired in a way that reveals global field symmetries (cf. Achilleos *et al.* 2000). Finally, our method can be employed in the reconstruction of flow fields by combining sparse data acquisition and computational fluid dynamics (Raguin *et al.* 2004).

The analytically reconstructed streamfunction for the SHV mode allows a methodical study of its kinematics. This permits the delineation of the three-dimensional flow skeleton, which consists of a pair of asymmetric helical counter-rotating vortices wrapped around the inner cylinder in the direction of the inner boundary rotation and separated by two counter-current annular flow streams (figure 6). The flow topology proposed in this study is consistent with general topological constraints, which exclude a number of other flow topologies, and is further corroborated by other independent experimental and numerical findings (cf. figure 7). The complete kinematic description in this study is a significant improvement over previous observations, which over-simplified the SHV mode by postulating that the flow is constituted by two identical counter-rotating vortices helically wound around the inner cylinder. First, it is shown that the SHV flow skeleton proposed here is structurally stable, unlike earlier simplistic

models. Second, the asymmetry of the two counter-rotating vortices is pointed out (and explained) for the first time. A transverse section of the flow such as in figures 4 and 10 reveals the shape taken by the two counter-rotating vortices (unlike in axisymmetric flows where only meridional sections intersect the vortices), and clearly demonstrates that the asymmetry in vortex size and strength is driven by the inner cylinder rotation.

Besides the aesthetic appeal of the SHV mode rendered in figure 6, the analytical reconstruction of a three-dimensional volume-preserving duct flow field has important consequences for the study of three-dimensional dynamic systems in the strongly nonlinear regime. The SHV mode constitutes a steady three-dimensional flow with zero inter-vortex mixing and minimum viscous dissipation relative to a class of oscillatory or propagating perturbed states having zero cylindrical average velocity ($\overline{u_z} = 0$). Introducing a second dilute phase into the SHV flow therefore suggests a candidate canonical problem for the study of dispersed-phase segregation in open chaotic flows, a topic which has received little attention relative to mixing and has recently been studied by Raguin (2004). Finally, we have shown rigorously that the phase portrait of the SHV mode corresponds to an integrable Hamiltonian system characterized by a plethora of critical features which would usher in rich chaotic phenomena when perturbed. This expectation is supported by experience with similar, albeit lower-dimension, dynamic systems or prototypical flows. The Hamiltonian perspective can indeed simplify the study of the global properties of these systems (cf. Salmon 1988). The study of the Lagrangian properties of these three-dimensional perturbed flows has to be postponed until appropriate dynamic constraints can be taken into consideration. Even for a single set of (*Re*, *Ta*) parameters, obtaining a high-resolution description for the SHV mode which obeys strict mass conservation is a requisite starting point for anyone pursuing such studies (cf. Raguin 2004; Raguin & Georgiadis 2004*b*).

The authors wish to acknowledge Dr K. W. Moser for contributing his expertise in MRI velocimetry. This project has been supported by DARPA (under contract DABT 63-98-C-0053) and by the NSF–Science & Technology CAMPWS (cooperative agreement CTS-0120978).

REFERENCES

Abraham, R., Marsden, J. E. & Ratiu, T. 1988 *Manifolds, Tensor Analysis, and Applications*, 2nd Edn. Springer.

Achilleos, E. C., Prud'homme, R. K., Christodoulou, K. N., Gee, K. R. & Kevrekidis, I. G. 2000 Dynamic deformation visualization in swelling of polymer gels. *Chem. Engng Sci.* **55**, 3335–3340.

Ameer, G. A., Barabino, G., Sasisekharan, R., Harmon, W., Cooney, C. L. & Langer, R. 1999 Ex vivo evaluation of a Taylor–Couette flow, immobilized heparinase I device for clinical application. *Proc. Natl Acad. Sci. USA* **96**, 2350–2355.

Ashwin, P. & King, G. P. 1995 Streamline topology in eccentric Taylor vortex flow. *J. Fluid Mech.* **285**, 215–247.

Ashwin, P. & King, G. P. 1997 A study of particle paths in non-axisymmetric Taylor–Couette flows. *J. Fluid Mech.* **338**, 341–362.

Bagrets, A. A. & Bagrets, D. A. 1997 Nonintegrability of two problems in vortex dynamics. *Chaos* **7**, 368–375.

Benczik, I. J., Toroczkai, Z. & Tel, T. 2002 Selective sensitivity of open chaotic flows on inertial tracer advection; Catching particles with a stick. *Phys. Rev. Lett.* **89**, 164501/1–164501/4.

Benjamin, T. B. 1978*a* Bifurcation phenomena in steady flows of a viscous fluid. I. Theory. *Proc. R. Soc. Lond.* A **359**, 1–26.

Benjamin, T. B. 1978*b* Bifurcation phenomena in steady flows of a viscous fluid. II. Experiments. *Proc. R. Soc. Lond.* A **359**, 27–43.

Bohl, D. G., Koochesfahani, M. M. & Olson, B. J. 2001 Development of stereoscopic molecular tagging velocimetry. *Exps. Fluids* **30**, 302–308.

Büchel, P., Lücke, M. & Schmitz, D. R. R. 1996 Pattern selection in the absolutely unstable regime as a nonlinear eigenvalue problem: Taylor vortices in axial flow. *Phys. Rev.* E **53**, 4764–4777.

Bühler, K. & Polifke, N. 1990 Dynamical behaviour of taylor vortices with superimposed flow. In *Nonlinear Evolution of Spatio-temporal Structures in Dissipative Continuous Systems*, pp. 21–29. Plenum.

Chandrasekhar, S. & Elbert, D. D. 1958 On orthogonal functions which satisfy four boundary conditions. III. Tables for use in Fourier–Bessel-type expansions. *Proc. R. Soc. Lond.* A **246**, 301–311.

Coles, D. 1965 Transition in circular Couette flow. *J. Fluid Mech.* **21**, 385–425.

Davey, A. 1962 The growth of taylor vortices in flow between rotating cylinders. *J. Fluid Mech.* **14**, 336–368.

Davey, A., DiPrima, R. C. & Stuart, J. T. 1968 On the instability of Taylor vortices. *J. Fluid Mech.* **31**, 17–52.

Drazin, P. G. & Reid, W. H. 1981 *Hydrodynamic Stability*. Cambridge University Press.

Giordano, R. C., Giordano, R. L. C., Prazeres, D. M. F. & Cooney, C. L. 1998 Analysis of a Taylor–Poiseuille vortex flow reactor – I: flow patterns and mass transfer characteristics. *Chem. Engng Sci.* **53**, 3635–3652.

Haim, D. & Pismen, L. M. 1994 Performance of a photochemical reactor in the regime of Taylor–Görtler vortical flow. *Chem. Engng Sci.* **49**, 1119–1129.

Hill, D. F., Sharp, K. V. & Adrian, R. J. 2000 Stereoscopic particle image velocimetry measurements of the flow around a Rushton turbine. *Exps. Fluids* **29**, 478–485.

Holdych, D. J. 2003 Lattice Boltzmann methods for diffuse and mobile interfaces. PhD thesis, University of Illinois at Urbana–Champaign.

Jana, S. C., Metcalfe, G. & Ottino, J. M. 1994 Experimental and computational studies of mixing in complex Stokes flows: the vortex mixing flow and multicellular cavity flows. *J. Fluid Mech.* **269**, 199–246.

Joseph, D. D. 1976 *Stability of Fluid Motions. 1. Fluid Dynamics*. Springer.

Lueptow, R. M., Docter, A. & Min, K. 1992 Stability of axial flow in an annulus with a rotating inner cylinder. *Phys. Fluids* A **4**, 2446–2455.

Ma, T. & Wang, S. 2000 Structural evolution of the Taylor vortices. *Math. Model. Numer. Anal.* **34**, 419–437.

Ma, T. & Wang, S. 2001 Structure of 2D incompressible flows with the Dirichlet boundary conditions. *Discrete Contin. Dyn. Syst.* B **1**, 29–41.

MacKay, R. S. 1994 Transport in 3D volume-preserving flows. *J. Nonlinear Sci.* **4**, 329–354.

Mezic, I. & Wiggins, S. 1994 On the integrability and perturbation of 3-D fluid flows with symmetry. *J. Nonlinear Sci.* **4**, 157–194.

Moser, K. W., Georgiadis, J. G. & Buckius, R. O. 2000*a* On the accuracy of EPI-based phase contrast velocimetry. *Magn. Reson. Imaging* **18**, 1115–1123.

Moser, K. W., Georgiadis, J. G. & Buckius, R. O. 2001*a* On the use of optical flow methods with spin-tagging Magnetic Resonance Imaging. *Annals Biomed. Eng.* **29**, 9–17.

Moser, K. W., Kutter, E. C., Georgiadis, J. G., Buckius, R. O., Morris, H. D. & Torczynski, J. R. 2000*b* Velocity measurements of flow through a step stenosis using Magnetic Resonance Imaging. *Exps. Fluids* **29**, 438–447.

Moser, K. W., Raguin, L. G. & Georgiadis, J. G. 2001*b* Tomographic study of helical modes in bifurcating Taylor–Couette–Poiseuille flow using Magnetic Resonance Imaging. *Phys. Rev.* E **64**, 016319/1–016319/5.

Moser, K. W., Raguin, L. G., Harris, A., Morris, H. D., Georgiadis, J. G., Shannon, M. & Philpott, M. 2000*c* Visualization of Taylor–Couette and spiral Poiseuille flows using a snapshot FLASH spatial tagging sequence. *Magn. Reson. Imaging* **18**, 199–207.

Ng, B. S. & Turner, E. R. 1982 On the linear stability of spiral flow between rotating cylinders. *Proc. R. Soc. Lond.* A **233**, 289–343.

Ottino, J. M. 1989 *The Kinematics of Mixing: Stretching, Chaos, and Transport*. Cambridge University Press.

Raguin, L. G. 2004 Theoretical and experimental study of a continuous hydrodynamically-enhanced separation system paradigm. PhD thesis, University of Illinois at Urbana-Champaign.

Raguin, L. G. & Georgiadis, J. G. 2004*a* Reduced-encoding method for MR phase contrast velocimetry using physical constraints. (In preparation).

Raguin, L. G. & Georgiadis, J. G. 2004*b* Segregation with chaotic swirling flows (in preparation).

Raguin, L. G., Kodali, A. K., Rovas, D. V. & Georgiadis, J. G. 2004 An inverse problem for reduced-encoding MRI velocimetry in potential flows. In *Proc. 26th Annu. Intl Conf. of the IEEE Engineering in Medicine and Biology Society, San Fransisco, Sept. 1–4, 2004.*

Raguin, L. G., Shannon, M. & Georgiadis, J. G. 2001 Radial and axial dispersion in Taylor–Couette and Poiseuille vortex flows. *Intl J. Heat Mass Transfer* **44**, 3295–3306.

Rothstein, D., Henry, E. & Gollub, J. P. 1999 Persistent patterns in transient chaotic fluid mixing. *Nature* **401**, 770–772.

Salmon, R. 1988 Hamiltonian fluid mechanics. *Annu. Rev. Fluid Mech.* **20**, 225–256.

Schwarz, K. W., Springett, B. E. & Donnelly, R. J. 1964 Modes of instability in spiral flow between rotating cylinders. *J. Fluid Mech.* **20**, 281–289.

Snyder, H. A. 1962 Experiments on the stability of spiral flow at low axial Reynolds numbers. *Proc. Roy. Soc.* A **265**, 198–214.

Snyder, H. A. 1969 Wave-number selection at finite amplitude in rotating Couette flow. *J. Fluid Mech.* **35**, 273–298.

Takeuchi, D. I. & Jankowski, D. F. 1981 A numerical and experimental investigation of the stability of spiral Poiseuille flow. *J. Fluid Mech.* **102**, 101–126.

Tsameret, A. & Steinberg, V. 1994 Competing states in a Couette–Taylor system with axial flow. *Phys. Rev.* E **49**, 4077–4086.

Watson, G. N. 1944 *A Treatise on the Theory of Bessel Functions*. Cambridge University Press.

Wereley, S. T. & Lueptow, R. M. 1999 Velocity field for Taylor–Couette flow with an axial flow. *Phys. Fluids* **11**, 3637–3649.

Wiggins, S. 1992 *Chaotic Transport in Dynamical Systems*. Springer.